



**HAL**  
open science

## Superiority of the Triple-Acting 5-HT<sub>6</sub>R/5-HT<sub>3</sub>R Antagonist and MAO-B Reversible Inhibitor PZ-1922 over 5-HT<sub>6</sub>R Antagonist Intepirdine in Alleviation of Cognitive Deficits in Rats

Katarzyna Grychowska, Uriel López-Sánchez, Mathieu Vitalis, Geoffrey Canet, Grzegorz Satala, Agnieszka Olejarz-Maciej, Joanna Gołębiowska, Rafal Kurczab, Wojciech Pietruś, Monika Kubacka, et al.

### ► To cite this version:

Katarzyna Grychowska, Uriel López-Sánchez, Mathieu Vitalis, Geoffrey Canet, Grzegorz Satala, et al.. Superiority of the Triple-Acting 5-HT<sub>6</sub>R/5-HT<sub>3</sub>R Antagonist and MAO-B Reversible Inhibitor PZ-1922 over 5-HT<sub>6</sub>R Antagonist Intepirdine in Alleviation of Cognitive Deficits in Rats. *Journal of Medicinal Chemistry*, 2023, 66 (21), pp.14928-14947. 10.1021/acs.jmedchem.3c01482 . hal-04235140

**HAL Id: hal-04235140**

**<https://hal.science/hal-04235140>**

Submitted on 28 Oct 2023

**HAL** is a multi-disciplinary open access archive for the deposit and dissemination of scientific research documents, whether they are published or not. The documents may come from teaching and research institutions in France or abroad, or from public or private research centers.

L'archive ouverte pluridisciplinaire **HAL**, est destinée au dépôt et à la diffusion de documents scientifiques de niveau recherche, publiés ou non, émanant des établissements d'enseignement et de recherche français ou étrangers, des laboratoires publics ou privés.



Distributed under a Creative Commons Attribution 4.0 International License

# Superiority of the Triple-Acting 5-HT<sub>6</sub>R/5-HT<sub>3</sub>R Antagonist and MAO-B Reversible Inhibitor PZ-1922 over 5-HT<sub>6</sub>R Antagonist Intepirdine in Alleviation of Cognitive Deficits in Rats

Katarzyna Grychowska, Uriel López-Sánchez, Mathieu Vitalis, Geoffrey Canet, Grzegorz Satała, Agnieszka Olejarz-Maciej, Joanna Gołębiowska, Rafał Kurczab, Wojciech Pietruś, Monika Kubacka, Christophe Moreau, Maria Walczak, Klaudia Blicharz-Futera, Ophélie Bento, Xavier Bantreil, Gilles Subra, Andrzej J. Bojarski, Frédéric Lamaty, Carine Becamel, Charleine Zussy, Séverine Chaumont-Dubel, Piotr Popik, Hugues Nury, Philippe Marin, Laurent Givalois, and Paweł Zajdel\*



Cite This: <https://doi.org/10.1021/acs.jmedchem.3c01482>



Read Online

ACCESS |



Metrics & More

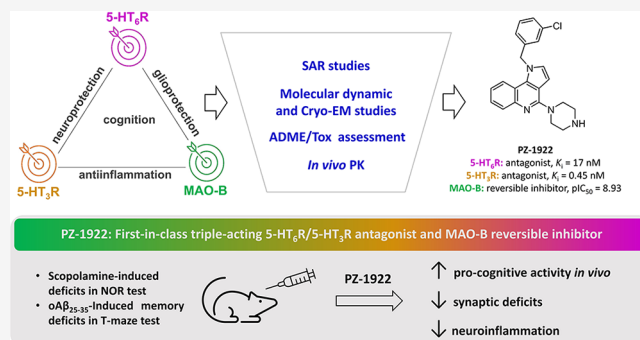


Article Recommendations



Supporting Information

**ABSTRACT:** The multifactorial origin and neurochemistry of Alzheimer's disease (AD) call for the development of multitarget treatment strategies. We report a first-in-class triple acting compound that targets serotonin type 6 and 3 receptors (5-HT<sub>6</sub>R) and monoamine oxidase type B (MAO-B) as an approach for treating AD. The key structural features required for MAO-B inhibition and 5-HT<sub>6</sub>R antagonism and interaction with 5-HT<sub>3</sub>R were determined using molecular dynamic simulations and cryo-electron microscopy, respectively. Bioavailable PZ-1922 reversed scopolamine-induced cognitive deficits in the novel object recognition test. Furthermore, it displayed superior pro-cognitive properties compared to intepirdine (a 5-HT<sub>6</sub>R antagonist) in the AD model, which involved intracerebroventricular injection of an oligomeric solution of amyloid- $\beta$  peptide ( $\alpha$ A $\beta$ ) in the T-maze test in rats. PZ-1922, but not intepirdine, restored levels of biomarkers characteristic of the debilitating effects of  $\alpha$ A $\beta$ . These data support the potential of a multitarget approach involving the joint modulation of 5-HT<sub>6</sub>R/5-HT<sub>3</sub>R/MAO-B in AD.



## INTRODUCTION

Alzheimer's disease (AD) patients suffer from progressive impairment of cognitive functions and emotional instability. At the molecular level, the development of AD is associated with the formation of amyloid- $\beta$  ( $A\beta$ ) plaques and  $\tau$  protein tangles, followed by a neuroinflammation process consecutive to the activation of astrocytes and microglia. These processes are accompanied by biological changes, including synaptic loss, neuronal death, and disturbances in neurotransmission.<sup>1</sup>

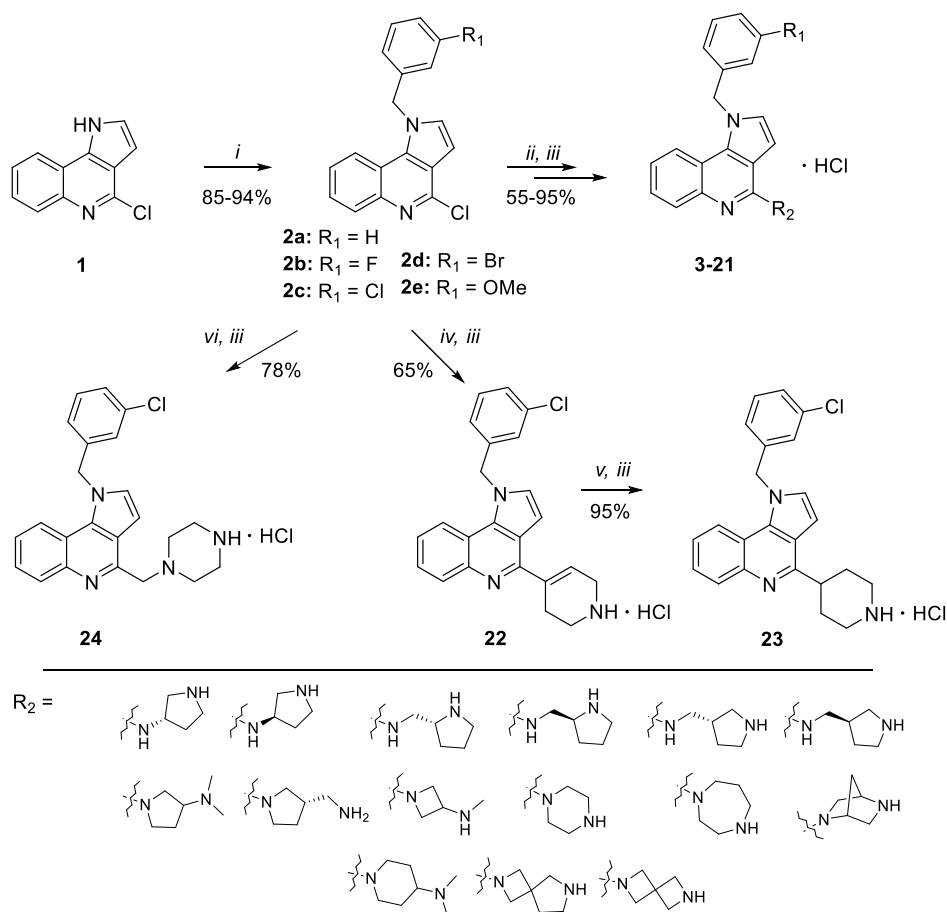
The recent fiasco of biological therapy in the treatment of AD, together with the multifactorial origin of neurodegenerative diseases such as AD, has led to the reevaluation of the strategies for small molecules research, from the conventional single-target concept to the development of pleiotropic agents. These compounds are designed to target two or more seemingly unrelated proteins, triggering intricate neurochemical changes that aim to overcome the therapeutic burdens of available drugs. Promising examples of such multitarget drugs include ladostigil,<sup>2</sup> which acts as a dual-acting inhibitor of acetylcholinesterase (AChE) and monoamine oxidase type B (MAO-B), as

well as donecopride,<sup>3</sup> a serotonin type 4 receptor agonist (5-HT<sub>4</sub>R) and AChE inhibitor. These compounds are currently undergoing preclinical or clinical evaluation as potential treatments for AD.

In this study, we conceptualized compounds capable of antagonizing 5-HT<sub>6</sub>R and 5-HT<sub>3</sub>R and inhibiting the activity of MAO-B as a novel strategy holding promise for treating AD. This is because 5-HT<sub>6</sub>R has a unique distribution in brain regions that are responsible for cognitive functions. In addition, preclinical data have demonstrated cognition-enhancing properties of 5-HT<sub>6</sub>R antagonists in rodent models of AD,<sup>4,5</sup> schizophrenia,<sup>6</sup> and neuropathic pain.<sup>7</sup> Additionally, a proof-

Received: August 11, 2023

Published: October 5, 2023

Scheme 1. Synthetic Pathway Leading to 1*H*-Pyrrolo[3,2-*c*]quinoline Derivatives 3–24<sup>a</sup>

<sup>a</sup>(i) BTPP (Phosphazene Base P1-*t*-Bu-tris(tetramethylene), Respective Benzyl Bromide, CH<sub>2</sub>Cl<sub>2</sub>, 36 °C, 12 h, Yield 85–94% (ii) Primary Amine, *t*-BuONa, BINAP (2,2'-Bis(diphenylphosphino)-1,1'-binaphthyl), Pd<sub>2</sub>(dba)<sub>3</sub> (Tris(dibenzylideneacetone)dipalladium(0)), Dioxane/*t*-BuOH 3/1, 90 °C, 1 h, MW or Secondary Amine, Acetonitrile, TEA, 140 °C, 7 h, MW, Yield 55–95% (iii) 1 M HCl/MeOH, rt, 12 h, Yield 95–99% (iv) 3,6-Dihydro-2*H*-pyridine-1-*N*-Boc-4-boronic Acid Pinacol Ester, Pd(dppf)Cl<sub>2</sub> ([1,1'-Bis(diphenylphosphino)ferrocene]dichloropalladium(II)), K<sub>2</sub>CO<sub>3</sub>, Water, 80 °C, 6 h, MW, Yield 65% (v) 10% Pd/C, Ethanol, rt, 2 h, Yield 95% (vi) Potassium ((4-(*tert*-Butoxycarbonyl)piperazin-1-yl)methyl)trifluoroborate, Pd[(C<sub>6</sub>H<sub>5</sub>)<sub>3</sub>P]<sub>4</sub> (Tetrakis(triphenylphosphine)palladium(0)), K<sub>2</sub>CO<sub>3</sub>, Dioxane/Water 90 °C, 5 h, Yield 78%.

of-concept clinical trial has confirmed the efficacy of intepirdine (a 5-HT<sub>6</sub>R antagonist) in alleviating cognitive deficits in AD. Based on these findings, we considered the blockade of 5-HT<sub>6</sub>R to be a relevant mechanism for the development of multitarget drugs in the context of AD.<sup>8–10</sup>

In AD patients, there is a notable loss of cholinergic neurons and a deficiency in acetylcholine in specific brain regions. Modulating 5-HT<sub>3</sub>R may help mitigate these issues. By blocking presynaptic 5-HT<sub>3</sub>Rs, the hyperactivity of mesolimbic dopamine and excessive release of  $\gamma$ -aminobutyric acid (GABA) can be inhibited, thus increasing cholinergic neurotransmission in the hippocampus and cortex. Additionally, the blockade of postsynaptic 5-HT<sub>3</sub>R located on GABAergic interneurons can enhance glutamatergic transmission,<sup>11–13</sup> thereby promoting cognitive functions. The blockade of 5-HT<sub>3</sub>R also induces anti-inflammatory and neuroprotective effects against A $\beta$ -induced neurotoxicity.<sup>14</sup>

Reversible inhibition of MAO-B, a flavin adenine dinucleotide (FAD)-dependent enzyme, located in glial cells and mainly expressed in the cortical and hippocampal regions of the brain, has recently been considered a valuable therapeutic approach for AD.<sup>15</sup> Preclinical studies demonstrated that reversible MAO-B inhibitors, as opposed to irreversible ones, can ameliorate

cognitive deficits in transgenic mice with APP/PS1 mutations following a 4 week treatment.<sup>16</sup> This positive effect could be explained by the contribution of MAO-B to GABA-ergic transmission. Irreversible MAO-B inhibitors activate diamine oxidase (DAO) to compensate for the loss of MAO-B activity. However, this mechanism can lead to GABA-mediated astrogliosis. In contrast, reversible inhibitors do not induce DAO-dependent compensatory mechanisms, thus avoiding the shortcomings associated with irreversible inhibitors.<sup>16</sup>

Through structure–activity studies within a group of 1*H*-pyrrolo[3,2-*c*]quinoline compounds, we identified compound **PZ-1922**, which exhibited antagonistic properties at both receptors, along with potent inhibitory activity at MAO-B. To understand the key structural motifs required for 5-HT<sub>6</sub>R antagonist properties and MAO-B inhibition,<sup>17</sup> we conducted *in silico* analysis. Additionally, the fragments required for the interaction with 5-HT<sub>3</sub>R were revealed by using cryo-electron microscopy (cryo-EM) imaging. **PZ-1922** displayed favorable oral absorption and penetration into the central nervous system (CNS). *In vivo*, it effectively reversed memory deficits induced by scopolamine (SCOP) in the novel object recognition (NOR) test in rats and demonstrated the ability to prevent A $\beta$ -induced memory decline in the T-maze test in both curative and

preventive approaches. The compound also affected various biochemical parameters associated with A $\beta$ -induced neuroinflammation, synaptic deficits, and apoptosis. These data demonstrate the potential of a multitarget approach that involves the simultaneous targeting of 5-HT<sub>6</sub>R, 5-HT<sub>3</sub>R, and MAO-B in the development of new anti-AD agents.

## RESULTS

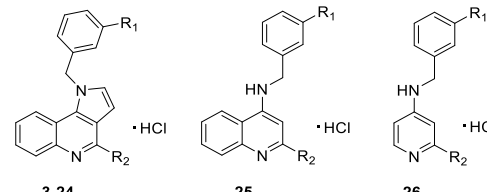
**Strategy Design and Summary of the Structure–Activity Relationship Studies.** Our design strategy relied on identifying the specific structural features required for 5-HT<sub>6</sub>R/5-HT<sub>3</sub>R antagonists<sup>10</sup> and selective reversible MAO-B inhibitors<sup>17</sup> within the 1*H*-pyrrolo[3,2-*c*]quinoline framework. To achieve this, we systematically diversified substituted benzyl fragments at the N<sup>1</sup> position and diverse alicyclic amine moieties at position C<sup>4</sup> of the central core. To synthesize the compounds, we adapted a function-oriented synthesis method previously developed for 4-chloro-1*H*-pyrrolo[3,2-*c*]quinoline (**1**) (Scheme 1).<sup>17</sup>

Briefly, alkylation of compound **1** with the respective benzyl bromides in the presence of BTTP yielded benzyl derivatives **2a–2e**. Subsequent coupling with primary amines under Buchwald–Hartwig *N*-arylation conditions provided compounds **3–12** (Table 1), while reactions with secondary amines, carried out under prolonged microwave heating in acetonitrile in the presence of triethylamine (TEA), yielded compounds **13–21**.<sup>17</sup> The 1,2,3,6-tetrahydropyridin-4-yl derivative **22** was synthesized by Suzuki coupling of 4-chloro-1-(3-chlorobenzyl)-1*H*-pyrrolo[3,2-*c*]quinoline **2c** with *N*-Boc-1,2,5,6-tetrahydropyridine-4-boronic acid pinacol ester, whereas its saturated congener **23** was obtained from **22** by reduction of the double bond using palladium on activated charcoal under a hydrogen atmosphere. Compound **24** was synthesized by coupling of **2c** with potassium salt of Boc-protected (piperazin-1-yl)-methyltrifluoroborate in the presence of tetrakis(triphenylphosphine)-palladium and K<sub>2</sub>CO<sub>3</sub>. This allowed us to access a series of 21 novel benzyl derivatives of 1*H*-pyrrolo[3,2-*c*]quinoline (**3–24**) that were modified with different alicyclic amines (Table 1 and Figure 1). Treatment of the obtained compounds with a 1 M HCl solution in methanol (MeOH) removed the Boc-protecting group and converted amine derivatives into their HCl salts (**3–24**). Additionally, two compounds (**25**, **26**) containing structurally simplified quinoline and pyridine cores (Figure 1) were synthesized (for detailed description, see Supporting Information, Scheme S1).

Our first goal was to verify the impact of the structural diversification on the affinity for 5-HT<sub>6</sub>R and the inhibitory activity at MAO-B. We aimed to identify compounds that exhibited dual activity within the nanomolar range, which would then be further evaluated for their activity at 5-HT<sub>3</sub>R. Among the various substituents at position 3 of the benzyl fragment (compounds **3–8**), the introduction of a chlorine atom proved to be the most favorable modification resulting in increased affinity for 5-HT<sub>6</sub>R and providing the most potent inhibitory activity at MAO-B.

The inclusion of different alicyclic amine fragments at position 4 of the 1*H*-pyrrolo[3,2-*c*]quinoline core, which are critical for affinity toward class A G-protein-coupled receptors (GPCRs), did not hamper the inhibitory activity at the MAO-B enzyme. The size and geometry of the alicyclic ring had an impact on the formation of a salt bridge between the basic center and the respective amino acid residue in the binding site of the

**Table 1. Affinity for 5-HT<sub>6</sub>R and Potency for MAO-B Inhibition of Synthesized Compounds 3–26 and Reference 5-HT<sub>6</sub>R Ligands and MAO-B Inhibitors**



Compd	R <sub>1</sub>	R <sub>2</sub>	K <sub>i</sub> ± SEM [nM] 5-HT <sub>6</sub> R <sup>a</sup>	pIC <sub>50</sub> ± SEM <sup>b</sup>
3	-H		21 ± 3	6.57 ± 0.03
4	3-F		21 ± 2	6.16 ± 0.05
5	3-Cl		7 ± 1	6.92 ± 0.04
6	3-Cl		30 ± 4	6.83 ± 0.01
7	3-Br		10 ± 1	6.89 ± 0.12
8	3-OMe		25 ± 3	6.86 ± 0.07
9	3-Cl		214 ± 26	5.70 ± 0.04
10	3-Cl		226 ± 30	6.52 ± 0.04
11	3-Cl		140 ± 18	8.02 ± 0.12
12	3-Cl		122 ± 10	6.52 ± 0.04
13	3-Cl		1339 ± 156	7.43 ± 0.04
14	3-Cl		1516 ± 220	8.00 ± 0.00
15	3-Cl		723 ± 87	8.22 ± 0.14
16 PZ-1922	3-Cl		17 ± 2	8.93 ± 0.00
17	3-Cl		138 ± 15	7.69 ± 0.12
18	3-Cl		372 ± 48	6.73 ± 0.02
19	3-Cl		1274 ± 173	5.60 ± 0.02
20	3-Cl		677 ± 82	7.01 ± 0.11
21	3-Cl		920 ± 127	6.97 ± 0.05
22	3-Cl		34 ± 4	6.67 ± 0.04
23	3-Cl		541 ± 80	6.13 ± 0.06
24	3-Cl		119 ± 14	5.21 ± 0.02
25	3-Cl		152 ± 18	5.36 ± 0.03
26	3-Cl		5448 ± 793	5.18 ± 0.04
Intepirdine			1.4 <sup>c</sup>	NT
Rasagiline			NT	7.72 ± 0.09
Safinamide			NT	8.05 ± 0.08

Table 1. continued

<sup>a</sup>Mean  $K_i$  values  $\pm$  SEMs (standard error of the mean) based on three independent binding experiments in HEK293 cells stably expressing *h*5-HT<sub>6</sub>R. <sup>b</sup>pIC<sub>50</sub> values  $\pm$  SEMs based on two experiments run in duplicate, determined by fluorometric method using human recombinant MAO-B and rasagiline [1  $\mu$ M] as a positive control. <sup>c</sup>Data taken from ref 18.

biological targets. This, in turn, determined the activity and selectivity of the compounds (Figure 1 and Table 1). It is worth noting that alicyclic amines with exocyclic amino groups (*N,N*-dimethylpyrrolidin-3-amine, (*S*)-pyrrolidin-3-ylmethanamine, *N*-methylazetidin-3-amine, and *N,N*-dimethylpiperidin-4-amine) were detrimental for binding to 5-HT<sub>6</sub>R (compounds 13, 14, 15, 19). However, alicyclic amines containing pyrrolidine and azetidine moieties (*N,N*-dimethylpyrrolidin-3-amine, (*S*)-pyrrolidin-3-ylmethanamine, *N*-methylazetidin-3-amine) showed potent inhibitory activity at MAO-B (compounds 13–15). On the other hand, spirocyclic amines did not exhibit favorable binding to either 5-HT<sub>6</sub>R or inhibition of MAO-B (compounds 20, 21).

Structure–activity relationship (SAR) evaluation revealed that the piperazine ring at the C<sup>4</sup> position of the 1*H*-pyrrolo[3,2-*c*]quinoline core was the only fragment that ensured the desired

pharmacological profile at both 5-HT<sub>6</sub>R and MAO-B and ( $K_i$  (5-HT<sub>6</sub>R) = 17 nM, pIC<sub>50</sub> (MAO-B) = 8.93).

To further demonstrate the role of the planar tricyclic scaffold in the interaction with both targets, we conducted experiments in which the fused pyrrole ring was removed from the pyrroloquinoline core (Table 1, Scheme S1). The resulting quinoline congener (25) exhibited a significant drop in affinity for 5-HT<sub>6</sub>R and reduced inhibitory activity at MAO-B. Furthermore, we performed additional structural simplification to obtain a compound (26) with a pyridine core. This compound was devoid of activity at both targets, indicating that the presence of the 1*H*-pyrrolo[3,2-*c*]quinoline core is required for dual action on both 5-HT<sub>6</sub>R and MAO-B (Figure 1).

**PZ-1922 Behaves as an Antagonist at 5-HT<sub>6</sub>R/5-HT<sub>3</sub>R and Reversibly Inhibits MAO-B.** Due to its potent and dual activity at 5-HT<sub>6</sub>R and MAO-B (Figure 2A,E), compound PZ-1922 was selected for further comprehensive evaluation. The high affinity of PZ-1922 for 5-HT<sub>6</sub>R translated well into potent antagonist properties when tested in 1321N1 cells expressing the human 5-HT<sub>6</sub>R ( $K_b$  = 33 nM, Figure 2B). 5-HT<sub>6</sub>R displays strong constitutive activity at Gs signaling in NG108-15 cells,<sup>19</sup> defined as spontaneous activity of the receptor in the absence of an agonist. This allows for the pharmacological differentiation of 5-HT<sub>6</sub>R antagonists for 5-HT<sub>6</sub>R inverse agonists, which can

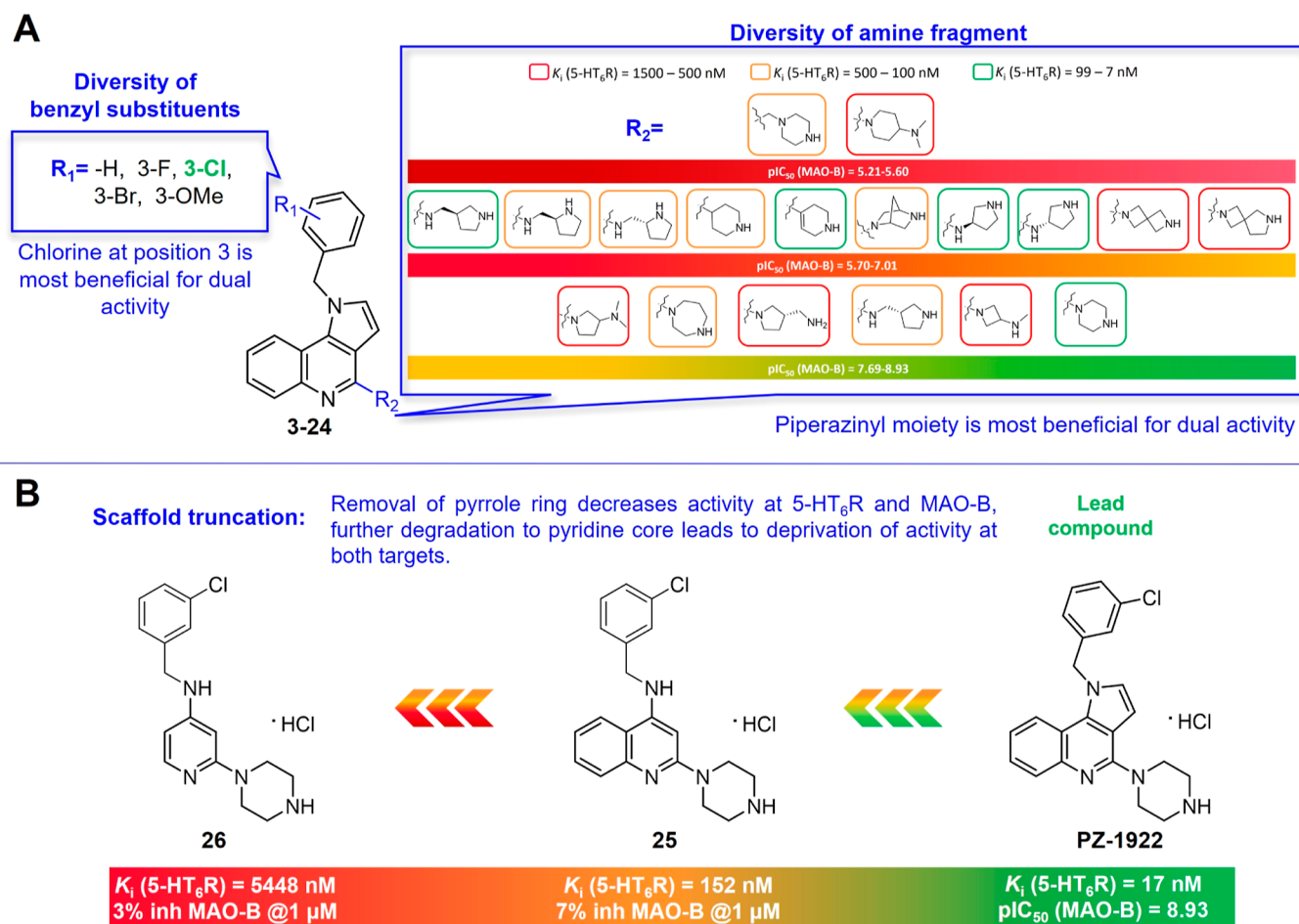


**Figure 1.** Summary of the SAR explored around 1*H*-pyrrolo[3,2-*c*]quinolines (3–24) and their molecular simplification analogues (25, 26) with a focus on inhibition of MAO-B and antagonism at 5-HT<sub>6</sub>R. (A) Structural diversity of benzyl substituents in the N<sup>1</sup> position and alicyclic amine fragments in the C<sup>4</sup> position. (B) 1*H*-Pyrrolo[3,2-*c*]quinoline as a privileged core for dual MAO-B inhibitory and 5-HT<sub>6</sub>R antagonistic properties.

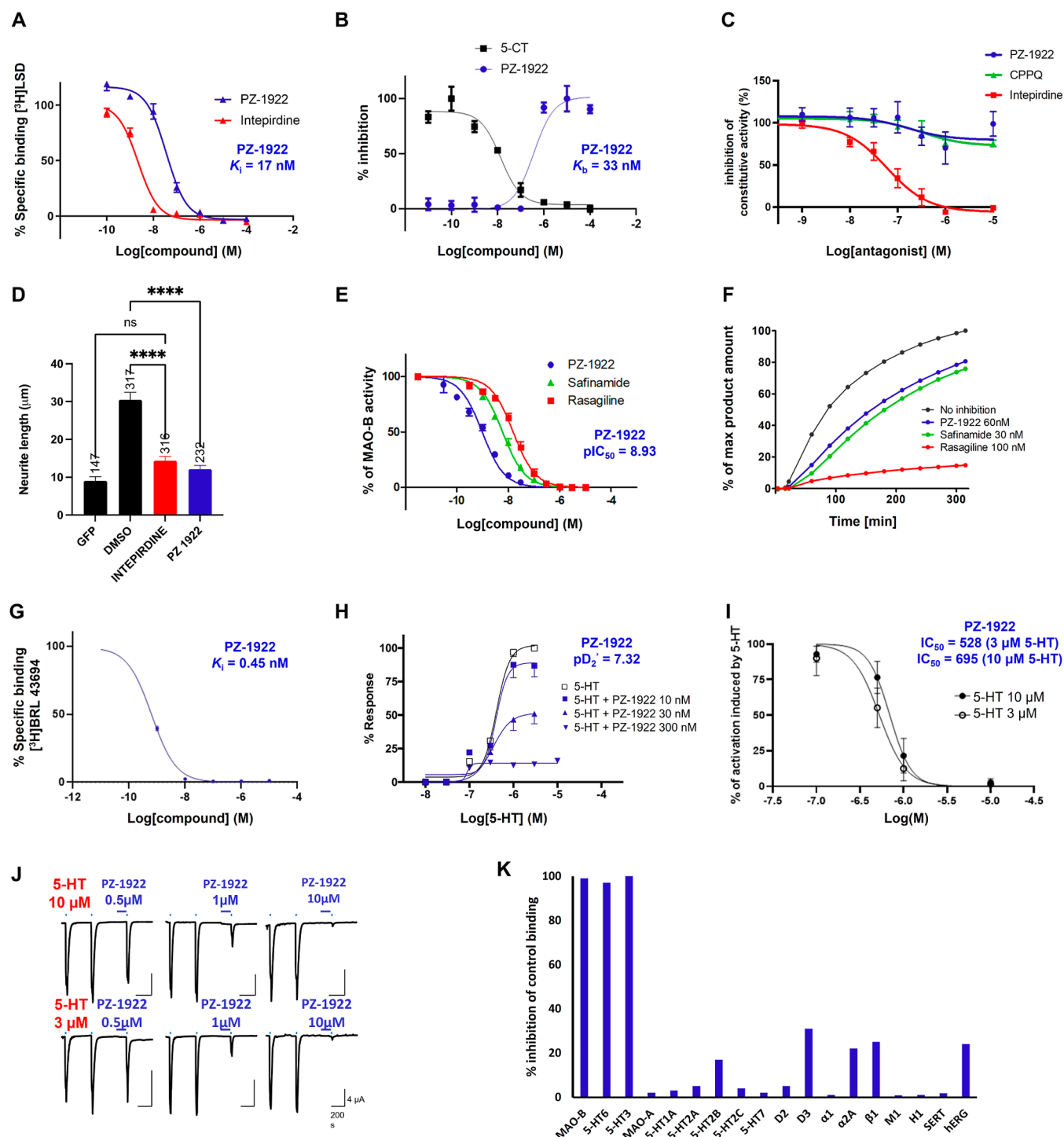


**Figure 2.** PZ-1922 behaves as a 5-HT<sub>6</sub>R/5-HT<sub>3</sub>R antagonist and MAO-B inhibitor. (A) PZ-1922 and intepirdine inhibit binding to 5-HT<sub>6</sub>R using 2 nM [ $^3\text{H}$ ]LSD in HEK cells stably expressing *h*5-HT<sub>6</sub>R.  $K_i$  value based on three independent binding experiments (SEM  $\leq 15\%$ ). (B) PZ-1922 increases cyclic AMP production elicited by an incremental concentration of 5-carboxamidotryptamine (5-CT) in 1321N1 cells.  $K_b$  value was calculated from the equation  $K_b = \text{IC}_{50}/(1 + A/\text{EC}_{50})$  where  $A$  is the agonist (5-CT) concentration used (1000 nM),  $\text{IC}_{50}$  is the concentration of antagonist producing a 50% reduction in response to the agonist, and  $\text{EC}_{50}$  (13 nM) is 5-CT concentration that causes a 50% maximal response. Data are means  $\pm$  SEM of the values obtained in three independent experiments (SEM  $\leq 22\%$ ). (C) PZ-1922, in contrast to intepirdine, does not impact 5-HT<sub>6</sub>R constitutive activity at Gs signaling in NG108-15 cells transiently expressing the human 5-HT<sub>6</sub>R. Cyclic AMP levels were estimated by using the CAMYEL BRET probe.<sup>22</sup> Data are the mean  $\pm$  SEM of the values obtained in three independent experiments performed in quadruplicate using different sets of cultured cells. (D) PZ-1922 and intepirdine inhibit the Cdk5-induced neurite growth in NG108-15 cells transiently expressing 5-HT<sub>6</sub>R. Cells were exposed to either vehicle, intepirdine (1  $\mu\text{M}$ ) or compound PZ-1922 (1  $\mu\text{M}$ ) for 24 h. The histogram shows the means  $\pm$  SEM of neurite length in each experimental condition measured in three independent experiments. \*\*\*\*  $p < 0.0001$  vs cells expressing 5-HT<sub>6</sub>R and treated with DMSO. (E) PZ-1922 inhibits MAO-B enzyme: inhibitor concentration–enzyme activity curve for PZ-1922 in the human recombinant MAO-B enzyme assay using the fluorometric method and 200  $\mu\text{M}$  p-tyramine as a substrate.  $\text{pIC}_{50}$  value calculated from two experiments run in duplicate (SEM  $< 1\%$ ). (F) PZ-1922 and safinamide behave as reversible MAO-B inhibitors and rasagiline as an irreversible inhibitor of MAO-B used at

Figure 2. continued

concentrations corresponding to their  $IC_{80}$  values in the presence of the substrate *p*-tyramine. Data present recovery of MAO-B activity after blockade with tested compound and represent means from two experiments performed in duplicate. (G) **PZ-1922** inhibits binding of the radioligand (0.5 nM [ $^3$ H]-BRL 43694) to 5-HT<sub>3</sub>R.  $K_i$  value was based on two independent binding experiments in human recombinant CHO cells expressing h5-HT<sub>3</sub>R ( $SEM \leq 15\%$ ). (H) **PZ-1922** displays antagonist properties at 5-HT<sub>3</sub>R, inhibiting serotonin-induced guinea pig ileum contractility. Responses are expressed as a percentage of maximal serotonin (5-HT) effect ( $E_{max} = 100\%$ ), reached in the concentration–response curves obtained before incubation with the tested compound. Each point represents the mean  $\pm$  SEM ( $N = 4$  to 8 trials,  $SEM \leq 6.6\%$ ). (I) **PZ-1922** inhibits the activity of 5-HT<sub>3</sub> heterologously expressed in *Xenopus* oocytes. Currents generated by 5-HT<sub>3</sub> are recorded by the two-electrode voltage-clamp (TEVC) technique. Dots are means  $\pm$  SEM of 5-HT<sub>3</sub> normalized activation by 5-HT after preincubation with **PZ-1922**. The number of tested oocytes per condition is between 4 and 8. (J) Representative TEVC recordings. Representative current traces measured for one concentration of **PZ-1922** and one concentration of 5-HT in one oocyte. (K) **PZ-1922** displays selectivity for 15 targets (at 1  $\mu$ M). A significant response (>50% inhibition) was obtained only for MAO-B, 5-HT<sub>6</sub>R, and 5-HT<sub>3</sub>R. Inhibition assay for MAO-A and binding assays for serotonin 5-HT<sub>1A</sub>R, 5-HT<sub>7</sub>R, and D<sub>2</sub>R were performed according to the previously reported methods.<sup>8,17</sup> Binding experiments for adrenergic  $\alpha_1$ R,  $\alpha_2A$ R, and  $\beta_1$ R, dopamine D<sub>3</sub>, histaminergic H<sub>1</sub>R, muscarinic M<sub>1</sub>R, serotonin 5-HT<sub>2A</sub>R, 5-HT<sub>2B</sub>R, 5-HT<sub>2C</sub>R, serotonin transporter SERT, and hERG channel were performed at Eurofins, France. For details, see [Supporting Information](#).

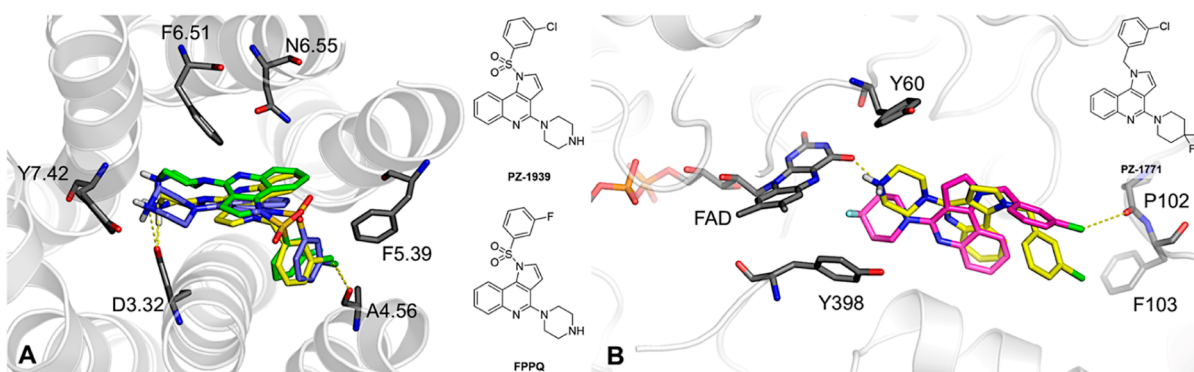


**Figure 3.** Illustrations of L-R complexes for 5-HT<sub>6</sub>R and MAO-B obtained by 100 ns-long MD simulations. (A) Comparison of binding modes of **PZ-1922** (yellow), **PZ-1939** (blue), and **FPPQ** (green) in 5-HT<sub>6</sub>R (PDB ID: 7XTB). (B) Comparison of binding modes of **PZ-1922** (yellow) and **PZ-1771** (magenta) in the MAO-B catalytic site (PDB ID: 2VSZ). Compounds **PZ-1939** (presented as **18**) and **FPPQ** were disclosed in ref **10**, compound **PZ-1771** refers to compound **26** from ref **17**.

inhibit spontaneous cAMP production (may inhibit both agonist-evoked and constitutive activity of the receptor), while neutral antagonists do not affect basal cAMP levels (may inhibit only agonist-evoked activity). In line with the prototypic 5-HT<sub>6</sub>R neutral antagonist CPPQ,<sup>20</sup> compound **PZ-1922** did not affect basal cAMP levels in NG108-15 cells expressing 5-HT<sub>6</sub>R, classifying it as a neutral antagonist at G<sub>s</sub> signaling (Figure 2C). In contrast, the well-characterized 5-HT<sub>6</sub>R inverse agonist intepirdine, used as a control, inhibited basal cAMP production in this model (Figure 2C). Furthermore, the constitutive activity of 5-HT<sub>6</sub>R at Cdk5 signaling can induce neurite growth and differentiation in NG108-15 cells.<sup>21</sup> In contrast to its neutral antagonist properties at G<sub>s</sub> signaling, **PZ-1922** exhibited similar efficacy as intepirdine in reducing neurite length in NG108-15 cells expressing 5-HT<sub>6</sub>R, indicating its inverse agonist activity at Cdk5 signaling (Figure 2D).

Similar to safinamide, **PZ-1922** demonstrated the reversible inhibition of MAO-B in kinetic studies performed using a fluorometric method. This reversible inhibition enabled a time-dependent recovery of the enzymatic activity of human recombinant MAO-B (Figure 2F).

**PZ-1922** also displayed a high affinity for human 5-HT<sub>3</sub>R (Figure 2G). It displayed potent antagonist properties at 5-HT<sub>3</sub>R, as evidenced by an ex vivo assay assessing guinea pig ileum contractility (with a  $pD_2'$  (**PZ-1922**) = 7.32, Figure 2H). The 5-HT<sub>3</sub>R antagonist properties of **PZ-1922** were further confirmed through electrophysiological recordings, which indicated its ability to inhibit 5-HT-induced inward currents in *Xenopus* oocytes expressing 5-HT<sub>3</sub>R (Figure 2I,J).

**PZ-1922** showed high selectivity over selected GPCRs (such as adrenergic  $\alpha_{2A}$ , dopamine D<sub>2</sub>, D<sub>3</sub> receptors, and serotonin 5-HT<sub>1A</sub>, 5-HT<sub>2A</sub>, 5-HT<sub>2C</sub>, and 5-HT<sub>7</sub>, as depicted in Figure 2K) in radioligand binding assays. It did not inhibit the MAO-A enzyme isoform, as assessed by the fluorometric method detecting the activity of human recombinant MAO-A (Figure 2K). Furthermore, **PZ-1922** demonstrated no potential adverse effects related to its affinity for the adrenergic  $\alpha_1$  receptor, adrenergic  $\beta_1$  receptor (which could be associated with hypertension or arrhythmia), D<sub>2</sub> dopamine receptor (linked to extrapyramidal symptoms and hyperprolactinemia), M<sub>1</sub> muscarinic receptor, and H<sub>1</sub> histaminic receptor (which could cause sedation). The cardiac safety of **PZ-1922** was based on its lack of effect on 5-HT<sub>2B</sub>R and the human Ether-à-go-go-Related Gene (hERG) channel, which are indicative of valvulopathy and prolongation of the QT interval, respectively.

**In Silico Evaluation of the Binding Mode of PZ-1922 at 5-HT<sub>6</sub>R and MAO-B.** The initial attempt to perform molecular docking of **PZ-1922** with the original crystal structures of 5-HT<sub>6</sub>R<sup>23</sup> and MAO-B<sup>24</sup> resulted in inconsistent results. This inconsistency was caused by conformational constraints of the binding site. To overcome these limitations, we used the induced-fit docking procedure. This allowed us to explore more flexible conformational states of the target proteins and obtain a stable form of the ligand complexes. In order to comprehensively analyze the selected SAR outcomes related to **PZ-1922**, we also included previously reported structural congeners from dual 5-HT<sub>6</sub>R/5-HT<sub>3</sub>R antagonists (**PZ-1939**, **FPPQ**),<sup>10</sup> as well as a class of selective MAO-B inhibitors (**PZ-1771**).<sup>17</sup>

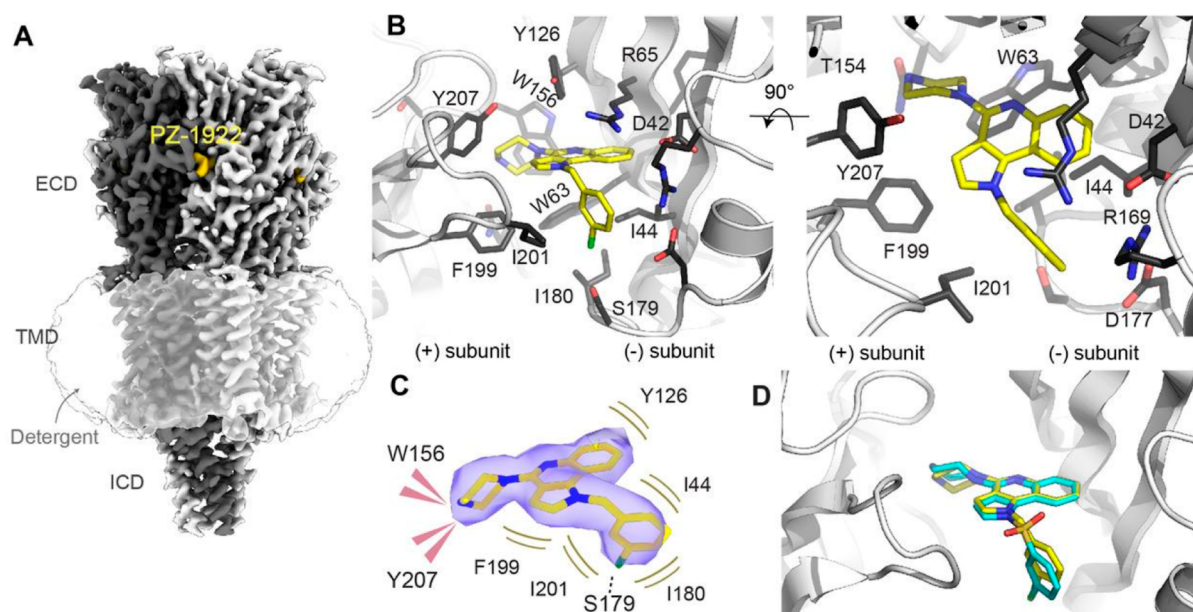


**Figure 4.** Structure of the mouse 5-HT<sub>3A</sub> receptor in complex with PZ-1922. (A) Cryo-EM representation of the overall structure of the receptor from the perspective of the membrane. (B) Side and top close-up views of the binding site, with PZ-1922 (PDB ID: 8CC6; EMDB ID: EMD-16555) in yellow sticks, and residues within 4.5 Å of it are depicted as sticks. In the top view, loop E side chains are removed for clarity. (C) Quality of the Coulombic potential map around PZ-1922 and schematic of the interaction between the drug and the receptor. (D) Superimposition with PZ-1939 (PDB ID: 8CC7; EMDB ID: EMD-16557). The drug positions are extremely similar, but in the case of PZ-1939 the density corresponding to the outer ring is not well-defined.

The effect of replacing a sulfonyl linker with a methylene one was examined in 5-HT<sub>6</sub>R comparing compounds PZ-1939 and PZ-1922. Similarly, the replacement of a gem-diF group with a basic center was investigated in MAO-B, comparing compounds PZ-1771 and PZ-1922. To evaluate the stability of the L–R complexes and analyze intermolecular interactions, 100 ns-long MD simulations were performed. The results were illustrated by using the geometrics of the L–R complexes obtained from the most frequently occurring MD trajectories, selected through trajectory clustering.

Upon analysis of the complexes of PZ-1922, PZ-1939, and FPPQ with 5-HT<sub>6</sub>R, a consistent pattern of L–R interactions at the binding site was observed. This included a salt bridge formation between the protonated piperazine nitrogen and the D3.32 side chain, CH $\cdots\pi$  interactions with F6.51, CH $\cdots\pi$  with F5.39, and a halogen bond with the carbonyl oxygen of A4.57 (Figure 3A). Further examination of the MD trajectories for PZ-1922 and PZ-1939 showed that the slightly lower affinity of PZ-1922 could be attributed to a reduced frequency of halogen bond (XB) formation with A4.56, compared to PZ-1939 (for detailed information, refer to the multivariate plots showing the dependency of the XB distance Cl $\cdots$ O versus the  $\sigma$ -hole angle C–Cl $\cdots$ O for each trajectory frame, Figure S1C). The methylene linker in PZ-1922 offered greater rotational freedom than the sulfonamide in PZ-1939, leading to increased rotatability of the entire benzyl group around the S–C/C–C bond (refer to the C1–N1–C2–C3 dihedral angles in Figure S1B). Additionally, quantum mechanical calculations were performed using a noncovalent interaction (NCI) approach to gain insight into the conformational preferences of PZ-1922 and PZ-1939 (Figure S1A). In the structure of PZ-1922, only a weak C–H $\cdots$ H attractive NCI was observed. Conversely, in PZ-1939, a series of S=O $\cdots$ H–C intramolecular hydrogen bonds between the benzyl and 1*H*-pyrrolo[3,2-*c*]quinoline moieties were observed (Figure S1A). These intramolecular hydrogen

bonds in PZ-1939 restricted its flexibility during MD simulations and positioned the 3-chlorobenzyl group favorably for additional stabilization of the L–R complex by the XB of A4.57.

Regarding MAO-B, PZ-1922 compared to its analogue lacking a basic center (PZ-1771) created an additional charge-assisted hydrogen bond with the cofactor FAD. Furthermore, cation $\cdots\pi$  interactions occurred between the protonated piperazine fragment and an “aromatic cage” composed of Y435, Y398, Y60, and F343. These crucial interactions properly positioned the ligand for interaction with FAD (Figure 3B).<sup>25,26</sup> The 3-chlorobenzyl fragment of the ligand was placed near the B entrance channel, and its position was stabilized by weak halogen bonds, with PZ-1922 forming a halogen bond with the ring centroid of F103, while PZ-1771 formed a halogen bond with the carbonyl oxygen of P102. It is worth mentioning that the created XBs stabilize the L–R complex (the dihedral angle in both cases is almost at a constant level, Figure S2B), despite the presence of weak intramolecular interactions between the 1*H*-pyrrolo[3,2-*c*]quinoline framework and the 3-chlorobenzyl fragment (as depicted in Figure S2A, showing only weak C–H $\cdots$ H and/or C–H $\cdots$ C interactions).

**Cryo-EM Structure of PZ-1922 Bound to 5-HT<sub>3A</sub>R.** Purified mouse 5-HT<sub>3A</sub>R was subjected to cryo-EM imaging in the presence of 10 mM PZ-1922 (Figure S3 and Table S1). A reconstruction of the receptor at 3.2 Å was obtained, revealing an extra density corresponding to the ligand within the binding site. The structure possesses the typical receptor features: a pentamer is organized around a central pseudosymmetrical axis that coincides with the ion pathway. The binding sites were located in the extracellular domain, specifically in the clefts between subunits (Figure 4A). The transmembrane domain contained the ion pore, which featured a closed hydrophobic gate (data not shown). The intracellular domain, which harbors an intrinsically disordered stretch, is partially resolved. The





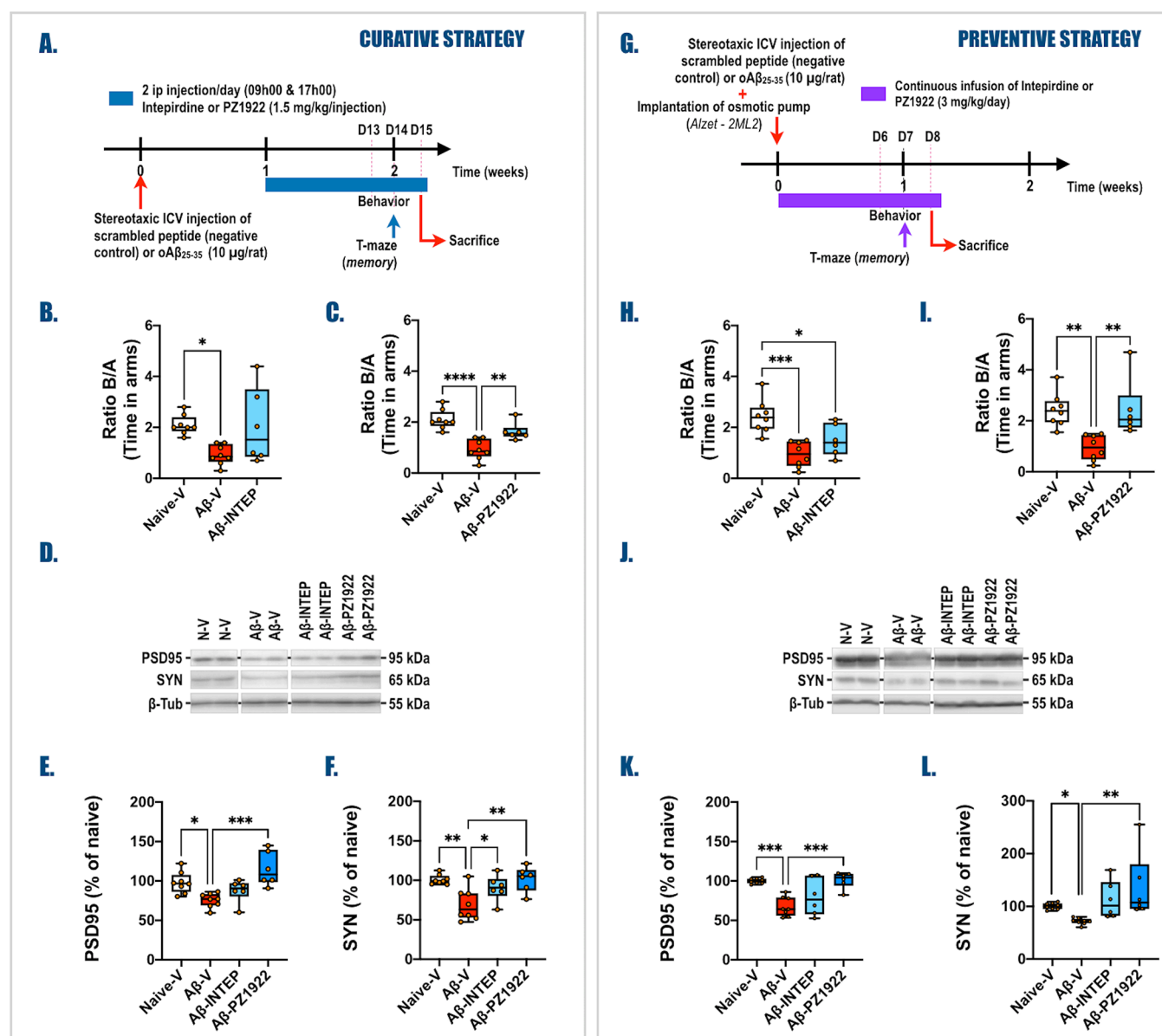


**Figure 7.** Impact of curative and preventive strategies using PZ-1922 (in comparison with intepirdine) on oAβ<sub>25-35</sub>-induced behavioral and synaptic alterations. (A) Curative experimental protocol—At T0, adult male rats (Sprague–Dawley) received any *icv* injection (Naive-V groups), an *icv* injection of oAβ<sub>25-35</sub> (10 μg/rat, Aβ groups), or an *icv* injection of Scrambled peptide (Scr groups). One week later, animals were subjected to treatment twice a day for 7 days (09:00 and 17:00) with an intraperitoneal (*ip*) injection of either vehicle (NaCl 0.9%, V groups), intepirdine (1.5 mg/kg/*ip* injection, INTEP groups), or PZ-1922 (1.5 mg/kg/*ip* injection, PZ-1922 groups). One day before the sacrifice (day 14), the spatial short-term memory of each rat was tested in the T-maze test. On the morning of day 15, the animals were sacrificed, and hippocampi were rapidly collected for Western blot analysis. (B,C) Spatial short-term memory performance was determined in the T-maze test after intepirdine (B) and PZ-1922 (C) treatments and expressed as the ratio of the time spent in the initially closed arm (B) to the time spent in the previous arm (A). (D–F) Variations of postsynaptic (PSD-95, 95 kDa, D,E) and presynaptic (SYN, 65 kDa, D,F) markers in the whole hippocampus were evaluated by Western blot in each group. (G) Preventive experimental protocol. At T0, adult male rats (Sprague–Dawley) received any *icv* injection (Naive groups), an *icv* injection of oAβ<sub>25-35</sub> (10 μg/rat, Aβ groups), or an *icv* injection of Scrambled peptide (Scr groups). In the same surgical procedure, osmotic pumps (Alzet, EML2) were implanted in intraperitoneal (*ip*), and either vehicle (NaCl 0.9%, V groups) or intepirdine (3 mg/kg/day, INTEP groups) or PZ-1922 (3 mg/kg/day, PZ-1922 groups) was delivered continuously during 1 week. One day before the sacrifice (day 7), the spatial short-term memory of each rat was tested in the T-maze test. The following day (day 8), the animals were sacrificed between 9:00 and 12:00, and hippocampi were rapidly collected for Western blot analysis. (H,I) Spatial short-term memory performance was determined in the T-maze test after intepirdine (H) and PZ-1922 (I) treatments and was expressed as the ratio of the time spent in the initially closed arm (B) over the time spent in the previous arm (A). (J–L) Expression of postsynaptic (PSD-95, 95 kDa, J,K) and presynaptic (SYN, 65 kDa, J,L) markers in the whole hippocampus were evaluated by Western blot in each group. All Western blot data were normalized to the respective variations of β-tubulin (β-tub, 55 kDa) and expressed in percent of values obtained in the noninjected Naive group. To simplify data, the Naive-V, Aβ-V, Aβ-INTEP, and Aβ-PZ-1922 groups were represented. Data for all other groups are available as Supporting Information (Figures S8 and S11). All data are presented as box and whiskers with Min to Max and Median  $n = 8$  for Naive-V and Aβ-V groups; and  $n = 6$  for Aβ-INTEP and Aβ-PZ-1922 groups. One-way ANOVA followed by a Tukey's or Dunnett's multiple comparison was performed (Table S4). \* $p < 0.05$ ; \*\* $p < 0.01$ ; \*\*\* $p < 0.001$ ; and \*\*\*\* $p < 0.0001$  vs selected group.

stabilized by hydrophobic interactions with F199, Y207, Y126, R75, I44, and W63. Furthermore, the chlorobenzyl fragment of the ligand resides at the entrance of the binding cavity, establishing hydrophobic interactions and potentially forming an H-bond with S179.

To compare the binding of two closely related compounds, we also performed cryo-EM imaging of m5-HT<sub>3</sub>R in the presence of 10 mM PZ-1939, resulting in a reconstruction with a resolution of 3.0 Å (Figure S4). The overall structure of the receptor and the binding pose of the ligand closely resemble those observed with PZ-1922 (Figure 4D). However, it is worth noting that the density corresponding to the most outward cycle of PZ-1939 appears fragmented, indicating a certain degree of flexibility (Figures S4 and S5). This observation can be attributed to the bulkier O=S=O linker in PZ-1939, which may hinder the complete capping of loop C (residues 199–207) and permit this flexibility. Furthermore, this finding supports the notion that the chlorobenzyl cycle of PZ-1922 plays a secondary role in its inhibitory effect on 5-HT<sub>3</sub>R (Figure S6).

**PZ-1922 is Brain Penetrant and Shows Favorable Bioavailability.** To investigate the preliminary pharmacokinetic characteristics of PZ-1922, its concentrations in plasma and brain were determined in male Wistar rats at various time points following oral (intragastric, *ig* administration, Figure 5 and Table S2) and intravenous (*iv*, Figure 5 and Table S2) administration at a dose of 3 mg/kg. PZ-1922 demonstrated the ability to penetrate the blood–brain barrier (BBB), as evidenced by a brain concentration ( $C_{\max}$ ) of  $129.6 \pm 9.49$  ng/g reached 4 h ( $T_{\max}$ ) after *ig* administration. The compound exhibited a decent half-life of approximately 6 h after *ig* administration and 13 h after *iv* administration. Notably, PZ-1922 displayed a high volume of distribution (*ca.* 42 L/kg), indicating high penetration throughout the body. Furthermore, it exhibited significant BBB penetration, as indicated by brain-to-plasma ratios of 3.14 (*ig*) and 6.10 (*iv*). The compound was characterized by high bioavailability ( $F = 48\%$ ) after *ig* administration. Overall, the study indicated that PZ-1922 possesses favorable pharmacokinetic properties for *in vivo* pharmacology studies.

**PZ-1922 Reverses Scopalamine-Induced Cognitive Impairment in the NOR Test.** Administration of SCOP, a muscarinic receptor antagonist, results in both short- and long-term memory impairment in the NOR test, which is often used to examine cognitive decline caused by alteration of cholinergic transmission. In the NOR test, when PZ-1922 was administered at varying doses (0.3, 1, and 3 mg/kg) 30 min prior to SCOP administration, it dose-dependently prevented the SCOP-induced deficits in short-term memory. Similarly, donepezil, an AChE inhibitor commonly used as a reference drug, also reduced the memory deficits induced by SCOP when administered at doses of 1 and 3 mg/kg (Figure 6).

**PZ-1922, Used as a Curative and Preventive Treatment, Abolishes A $\beta$ -Induced Memory Deficits in the T-Maze Test.** Accumulation of A $\beta$  oligomers in AD leads to synaptic disruption and progressive neuronal cell death. In AD patients, A $\beta$  oligomers primarily consist of A $\beta$ <sub>1–40</sub> and A $\beta$ <sub>1–42</sub> peptides,<sup>29</sup> along with shorter sequences such as A $\beta$ <sub>25–35</sub> or A $\beta$ <sub>25–35/40</sub>,<sup>30,31</sup> resulting from enzymatic cleavage of A $\beta$ <sub>1–40</sub>.<sup>30,31</sup> These shorter peptides contain extracellular and transmembrane residues, including a biologically active region of A $\beta$ <sup>32,33</sup> and a highly hydrophobic region that facilitates the formation of stable aggregates. Notably, the undecapeptide A $\beta$ <sub>25–35</sub>, which exhibits better solubility and higher efficacy, induces neurite atrophy, neuronal cell death, synaptic loss, as well as synaptic plasticity

and memory deficits, similarly to A $\beta$ <sub>1–40</sub> and A $\beta$ <sub>1–42</sub>.<sup>34</sup> To investigate the impact of PZ-1922 and intepirdine on A $\beta$ -induced memory deficits, we performed intracerebroventricular (*icv*) injection of a solution containing A $\beta$ <sub>25–35</sub> oligomers (oA $\beta$ <sub>25–35</sub>) in rats.<sup>35,36</sup> Subsequently, we examined the effects of PZ-1922 and intepirdine on these memory deficits (Figure 7).

In the curative approach, the tested compounds (intepirdine and PZ-1922) were administered 1 week after the induction of amyloid toxicity (*icv* injection of oA $\beta$ <sub>25–35</sub>). The administration involved two *ip* injections per day for 1 week, with each injection containing 1.5 mg/kg of the respective compound (Figure 7A). Fourteen days after the oA $\beta$ <sub>25–35</sub> injection, a behavioral memory test (T-maze) was performed (Figure 7A).

In the preventive approach, the tested compounds were administered simultaneously with the induction of A $\beta$  toxicity. This involved the *icv* injection of oA $\beta$ <sub>25–35</sub> and concurrent implantation of an osmotic pump (Alzet-EML2, Charles-River, France). The osmotic pump continuously delivered the compounds at a dose of 3 mg/kg/day for 1 week (Figure 7G). One week after the beginning of the treatment (day 7), the animals underwent the T-maze test.

The administration of PZ-1922 1 week after the oA $\beta$ <sub>25–35</sub> injections effectively reversed the memory deficits induced by amyloid toxicity in the T-maze test, demonstrating its curative effect (Figures 7C and S8B). On the other hand, intepirdine only partially reversed the memory deficits in this experimental paradigm (Figures 7B and S8A). Similarly, when administered concomitantly with oA $\beta$ <sub>25–35</sub>, PZ-1922 (Figure 7G) prevented the emergence of cognitive deficits, while intepirdine did not exhibit the same preventive effect (Figures 7H,I and S11B).

**PZ-1922 Impacts the Level of AD Biomarkers Associated with Synaptic Integrity, Cdk5 Activity, and Neuroinflammation.** Having established the beneficial effect of a triple inhibitory approach targeting 5-HT<sub>6</sub>/5-HT<sub>3</sub>/MAO-B on SCOP-induced and A $\beta$ -induced memory decline, our next step was to evaluate the impact of PZ-1922 and intepirdine on biomarkers associated with synaptic integrity (postsynaptic density protein 95—PSD-95, synaptotagmin—SYN), apoptosis (caspase type 3—Casp 3), Cdk5 activity (Cdk5, p22/p35), and neuroinflammation (glial fibrillary acidic protein—GFAP, ionized calcium-binding adaptor molecule 1—Iba1) in the hippocampus of rats injected with oA $\beta$ <sub>25–35</sub>. We assessed these biomarkers by performing Western blotting analysis on proteins extracted from the hippocampus of animals treated with curative and preventive approaches involving PZ-1922 and intepirdine.

Injection of oA $\beta$ <sub>25–35</sub> produced alterations in hippocampal synapses, as evidenced by a decrease in PSD-95 and SYN levels (Figure 7D–F,J–L). PZ-1922 reversed PSD-95 and SYN levels when administered as a curative or preventive treatment (Figures 7D–F,I–K, S8D,F, and S11D,F). In contrast, intepirdine reversed only the SYN level in the curative experimental paradigm (Figures 7D,F, S8C,E, and S11C,E).

The synaptic effects of oA $\beta$ <sub>25–35</sub> are also accompanied by cell death and progressive apoptosis, as indicated by an increased expression of Caspase-3 and Pro-caspase-3.<sup>37,38</sup> Both PZ-1922 and intepirdine decreased expression of Caspase-3 and Pro-caspase-3 when employed in a curative strategy (Figures S7A,C and S10E,H), and prevented increased expression of Caspase-3 and Pro-caspase-3 when administered as a preventive treatment (Figures S7D,F and S13E–I,H).

Further analysis focused on the effect of PZ-1922 and intepirdine on Cdk5 expression in the hippocampus of A $\beta$ -injected rats. Apart from its coupling to 5-HT<sub>6</sub>R, which enables

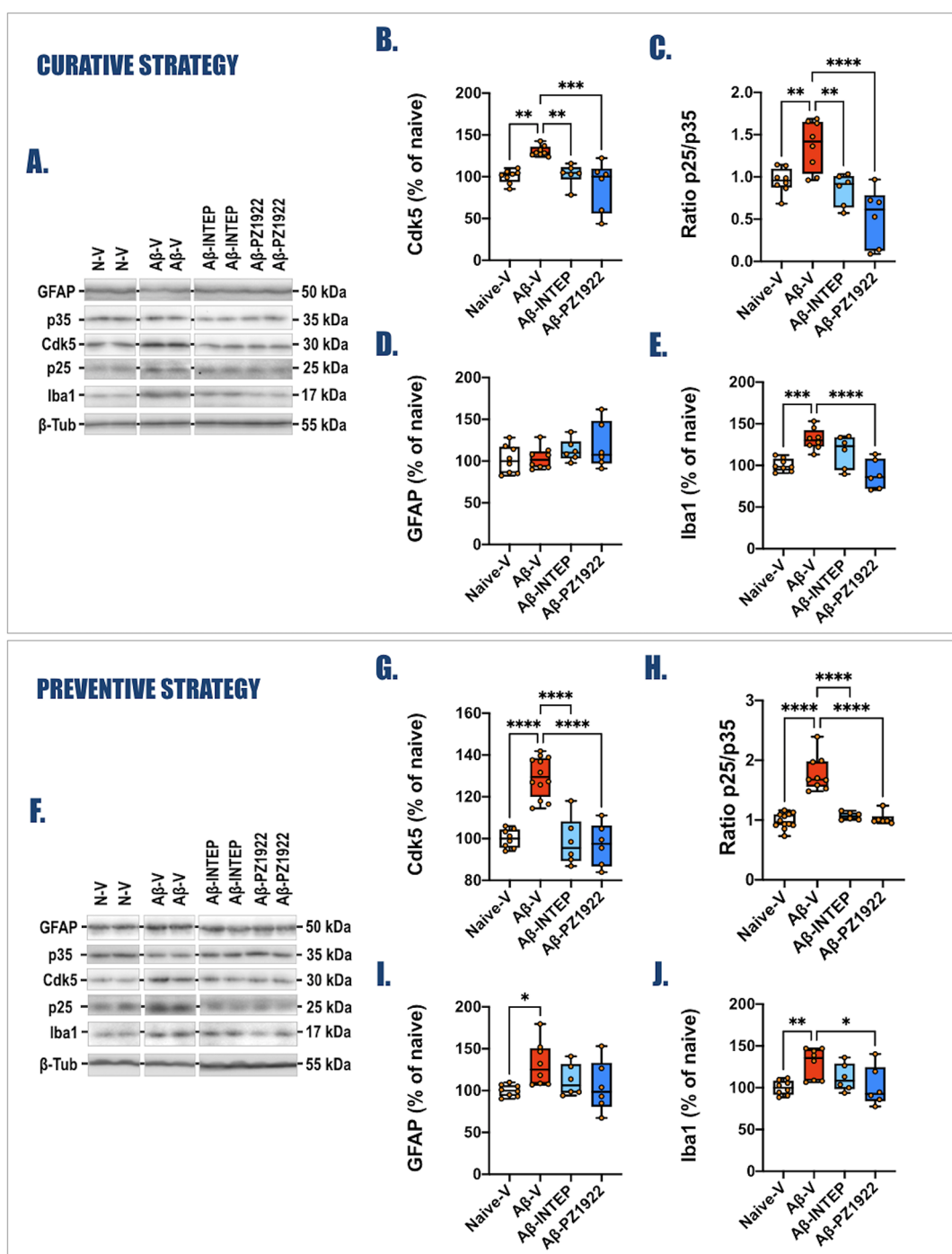


**Figure 8.** Impact of the curative and preventive treatments with intepirdine and PZ-1922 on specific AD markers induced by the *icv* injection of  $\alpha$ A $\beta_{25-35}$  was evaluated by Western blot analysis of hippocampal proteins. Variations of Cdk5 activity (Cdk5, 30 kDa; and the ratio of p25/p35, 25/35 kDa) (panels (A–C) for curative strategy and (F–H) for preventive strategy) and neuroinflammation (GFAP, 50 kDa; and Iba1, 17 kDa) (panels (A,D,E) for curative strategy and (F,I,J) for preventive strategy) were evaluated in each group, normalized using  $\beta$ -tubulin expression ( $\beta$ -tub, 55 kDa). Results are expressed as the percentage of variations compared to noninjected rats (Naive group). For experimental protocol, see Figure 6A (Curative) and 6G (Preventive). To simplify data, only the Naive-V, A $\beta$ -V, A $\beta$ -INTEP, and A $\beta$ -PZ-1922 groups were represented. Data for all other groups are available as Supporting Information (Figures S8–S10 and S11–S13). All data are presented as box and whiskers with Min to Max and Median with  $n = 8$  for Naive-V and A $\beta$ -V groups; and  $n = 6$  for A $\beta$ -INTEP and A $\beta$ -PZ-1922 groups. One-way ANOVA followed by Dunnett's multiple comparison was performed (Table S4). \* $p < 0.05$ ; \*\*\* $p < 0.001$ , and \*\*\*\* $p < 0.0001$  vs  $\alpha$ A $\beta_{25-35}$  group treated with vehicle (A $\beta$ -V).

the regulation of neurite growth,<sup>21,39,40</sup> Cdk5 activity is dependent on its association with the neuron-specific activators p35 and p39, as well as their truncated forms p25 and p29. Aberrant overactivation of Cdk5 occurs through the conversion of p35 to p25, leading to the formation of the Cdk5-p25

complex. This complex hyperphosphorylates Tau protein and indirectly increases amyloid production by stimulating BACE1.

The *icv* injection of  $\alpha$ A $\beta_{25-35}$  induced an increase in Cdk5 expression (Figure 8A,B,F,G) and an elevated conversion of p35 to p25 (Figure 8A,C,F,H). Both PZ-1922 and intepirdine

reduced the level of Cdk5 overexpression and the level of p25 protein and p25/p35 ratio in curative treatment (Figures 8 and S9). Moreover, PZ-1922 and intepirdine decreased the Cdk5 overexpression, the level of p25 protein, and p25/p35 ratio and restored the level of p35 protein when applied in preventive treatment approach (Figures 8 and S12).

Since astrocyte activation and recruitment of microglia contribute to the neuroinflammatory processes, we next assessed the hippocampal GFAP and Iba1. As previously reported,<sup>37,38,41</sup> we observed a transient activation of astrocytes only 1 week after the *icv* injection of  $\alpha\text{A}\beta_{25-35}$ , as demonstrated by the increased level of GFAP in the preventive approach (Figures 8A,D,F,I, S10A,B, S13A,B). This was followed by a sustained recruitment of microglial cells (Figures 8A,E,F,J, S10C,D, and S13C,D). It is worth noting that GFAP expression was no longer elevated 2 weeks after the *icv* injection of  $\alpha\text{A}\beta_{25-35}$  in the curative approach. Neither PZ-1922 nor intepirdine impacted the GFAP increase (Figure 8D,I). In contrast to intepirdine, PZ-1922 decreased the Iba1 level regardless of the applied approach (Figure 8E,J).

## DISCUSSION AND CONCLUSIONS

The emerging consensus regarding the multifactorial nature of AD has prompted a shift in small-molecule drug discovery strategies from single-target to multitarget approaches. In this study, we considered the combination of 5-HT<sub>6</sub>R/5-HT<sub>3</sub>R antagonism and inhibition of MAO-B as a promising approach to address the complex processes underlying cognition and degeneration in AD.

The rationale for this approach originated from behavioral studies revealing that antagonism at 5-HT<sub>6</sub>R alleviates cognitive deficits through the corticolimbic release of acetylcholine and glutamate achieved by blocking 5-HT<sub>6</sub>Rs located on GABAergic neurons. Moreover, ondansetron, a 5-HT<sub>3</sub>R antagonist, has already displayed pro-cognitive properties in clinical studies, and the neuroprotective effects of 5-HT<sub>3</sub>R antagonists found in *in vitro* and *in vivo* experiments further supported the inclusion of 5-HT<sub>3</sub>R antagonism in our multitarget approach. Considering the beneficial effects of lazabemide (a reversible MAO-B inhibitor) in a phase III clinical trial for AD, and the potential of reversible MAO-B inhibition to attenuate astrogliosis and enhance synaptic transmission,<sup>16</sup> reversible MAO-B inhibition holds promise for modulating neurodegenerative and neuroinflammatory processes in AD.

We thus explored the concept of the merged ligands to identify a novel compound, 1-(3-chlorobenzyl)-4-(piperazine-1-yl)-1*H*-pyrrolo[3,2-*c*]quinoline (PZ-1922), as a potential treatment for AD (Figure 1). PZ-1922 exhibited antagonistic activity at both 5-HT<sub>6</sub>R and 5-HT<sub>3</sub>R, as well as potent reversible inhibition of MAO-B. In contrast to the 5-HT<sub>6</sub>R inverse agonist intepirdine, it exhibited neutral antagonistic properties at 5-HT<sub>6</sub>R-mediated Gs signaling and behaved as an inverse agonist at Cdk5 signaling induced by constitutively active 5-HT<sub>6</sub>Rs (Figure 2).

Molecular dynamic simulations of PZ-1922, along with its dual-acting 5-HT<sub>6</sub>R/5-HT<sub>3</sub>R antagonist (PZ-1939) and selective MAO-B inhibitor (PZ-1771), revealed structural determinants that allowed simultaneous 5-HT<sub>6</sub>R antagonism and MAO-B inhibition. Cryo-EM confirmed the fragments required for interaction with 5-HT<sub>3</sub>R. Subsequent experiments using full-length mouse 5-HT<sub>3</sub>R demonstrated that the binding structure of PZ-1922 resolved at 3.2 Å resembled that of palonosetron.

The progressive memory decline characterizing AD is associated with the loss of cholinergic neurons and synapses and a decrease in ACh levels in brain regions involved in cognitive functions. To study the impact of altered cholinergic transmission on cognitive decline, we examined the compound's efficacy in reversing scopolamine-induced amnesia and demonstrated that PZ-1922 mimicked the pro-cognitive effects of clinically used donepezil in the NOR test (Figure 6).

In the  $\text{A}\beta$ -induced memory deficit model in rats, which involved *icv* injection of  $\alpha\text{A}\beta_{25-35}$ , PZ-1922 exhibited pro-cognitive properties in both curative and preventive paradigms. Importantly, in the latter model, PZ-1922 demonstrated superior efficacy compared to intepirdine, which acts solely as a 5-HT<sub>6</sub>R antagonist. These data suggest that the combined antagonism at 5-HT<sub>6</sub>R and 5-HT<sub>3</sub>R, along with the inhibitory activity at MAO-B, enhances the effectiveness of 5-HT<sub>6</sub>R antagonism alone in mitigating  $\text{A}\beta$ -induced memory deficits.

As previously reported,<sup>38,41</sup> behavioral changes induced by  $\alpha\text{A}\beta_{25-35}$  were accompanied by alterations in hippocampal synapses, as evidenced by a decrease in PSD-95 and SYN levels (Figure 7D–F,J–L). When administered as a curative or preventive treatment, PZ-1922 effectively reversed and prevented both postsynaptic and presynaptic deficits (Figure 7D,E,J,K). In contrast, intepirdine showed efficacy only at the presynaptic level and solely in the curative experimental paradigm (Figure 7D,F). These observations are in line with the results of the behavioral studies, indicating that compound PZ-1922 displays both curative and preventive effects, while intepirdine is only partially effective in the curative approach.

Multiple pieces of evidence support the correlation between Cdk5 overactivity and the pathogenesis of AD. Consistent with previous data,<sup>41,42</sup> the *icv* injection of  $\alpha\text{A}\beta_{25-35}$  induced an increase in Cdk5 expression (Figure 8A,B,F,G) and an elevated conversion of p35 to p25 (Figure 8A,C,F,H), ultimately leading to Cdk5 overactivation. Our findings demonstrate that both PZ-1922 and intepirdine effectively blocked Cdk5 activation in the hippocampus, regardless of the preventive or curative approach (Figures 8, S9, and S12).

The progression of AD is also associated with sustained neuroinflammation resulting from the activation of astrocytes, known as “reactive astrogliosis”, and the recruitment of microglia. Markers of microglia and astrocytes are elevated in AD patients and colocalized with  $\text{A}\beta$  plaques.<sup>37,38,41,43</sup> Therefore, we examined the levels of the reactive astrocyte marker GFAP and the microglial marker Iba1 in the hippocampus. PZ-1922, but not intepirdine, effectively abolished the neuroinflammatory response triggered by the administration of  $\alpha\text{A}\beta_{25-35}$  in both the curative and preventive approaches (Figures 8, S10, and S13).

In conclusion, we demonstrate that simultaneous blockade of 5-HT<sub>6</sub>R and 5-HT<sub>3</sub>R, along with inhibitory activity at MAO-B, enhances the effectiveness of 5-HT<sub>6</sub>R antagonism alone in the alleviation of cognitive deficits in rats. The present results further confirm the superiority of PZ-1922 over intepirdine (a 5-HT<sub>6</sub>R antagonist) in preventing and alleviating the molecular and synaptic alterations, as well as modulating neuroinflammatory processes in the hippocampus of  $\text{A}\beta$ -injected rats. The properties of PZ-1922 highlight the promising potential of simultaneously targeting 5-HT<sub>6</sub>R, 5-HT<sub>3</sub>R, and MAO-B as a novel approach for the development of anti-AD agents.

## EXPERIMENTAL SECTION

**Synthesis General Information.** The synthesis was conducted at room temperature unless indicated otherwise. Organic solvents (from Sigma-Aldrich and Chempur) were reagent grade and used without purification. All reagents (Sigma-Aldrich, Fluorochem, and TCI) were of the highest purity. Column chromatography was performed on silica gel Merck 60 (70–230 mesh ASTM).

UPLC analyses and high-resolution mass spectra (LC-HRMS) were obtained on a Waters ACQUITY I-Class PLUS SYNAPT XS high-resolution mass spectrometer (Waters, Milford, CT, USA) with the MS-Q-TOF detector and UV-VIS-DAD *el* detector. The ACQUITY UPLC BEH C18, 1.7  $\mu\text{m}$  (2.1  $\times$  100 mm) column was used with the VanGuard Acquity UPLC BEH C18, 1.7  $\mu\text{m}$  (2.1  $\times$  5 mm) (Waters, Milford, CT, USA). Standard solutions (1 mg/mL) of each compound were prepared in analytical grade MeCN/water mixture (1:1; v/v). Conditions applied were as follows: eluent A (water/0.1% HCOOH), eluent B (MeCN/0.1% HCOOH), a flow rate of 0.3 mL/min, a gradient of 5–100% B over 13 min, and an injection volume of 1  $\mu\text{L}$ . The UPLC/MS purity of all test compounds and key intermediates was determined to be >95%.

Elemental analysis for C, H, N, and S was performed on the elemental Vario EI III Elemental Analyzer (Hanau, Germany). All values are reported as percentages and were within  $\pm 0.4\%$  of the calculated values.

$^1\text{H}$  NMR and  $^{13}\text{C}$  NMR spectra were recorded using JEOL JNM-ECZR S00 RS1 (ECZR version) at 500 and 126 MHz, respectively, and are reported in ppm using deuterated solvent for calibration ( $\text{CDCl}_3$ , methanol- $d_4$  or  $\text{dmsO}-d_6$ ). The *J* values are given in Hertz (Hz). Melting points were determined with a Büchi apparatus and are uncorrected.

Spectral data for the final compounds **3**, **4**, **6**, **7–9**, **11–15**, **17–19**, **21**, **22**, and **24–26** are included in the [Supporting Information](#).

**General Procedure for Preparation of Compounds 3–12.** Respective compound **2a–2e** (0.52 mmol, 1 equiv) was mixed together with  $\text{Pd}_2(\text{dba})_3$  (10 mg, 0.010 mmol, 0.02 equiv), BINAP (13 mg, 0.021 mmol, 0.04 equiv), and *t*-BuONa (70 mg, 0.73 mmol, 1.4 equiv). The solids were suspended in 4 mL of a mixture of dioxane and *t*-BuOH (3/1, v/v), and the respective primary amine (1.2 equiv) was added. The reaction was irradiated with microwaves at 90  $^\circ\text{C}$  for 1 h under argon atmosphere. The resulting mixture was filtrated through a pad of Celite, concentrated, and purified by column chromatography on silica gel using  $\text{CH}_2\text{Cl}_2/\text{MeOH}$  as a developing solvent. The obtained product was converted into HCl salt of secondary amine upon overnight treatment with 1 M methanolic solution of HCl and subsequent filtration.

**(S)-1-(3-Chlorobenzyl)-N-(pyrrolidin-3-yl)-1H-pyrrolo[3,2-c]quinolin-4-amine Hydrochloride 5.** White solid, overall yield 60%,  $t_{\text{R}} = 4.47$  min, mp 181–183  $^\circ\text{C}$ ,  $\text{C}_{22}\text{H}_{22}\text{Cl}_2\text{N}_4$ , MW 413.35.  $^1\text{H}$  NMR (500 MHz, methanol- $d_4$ ):  $\delta$  ppm 2.34–2.48 (m, 1H), 2.58–2.75 (m, 1H), 3.50–3.58 (m, 1H), 3.63–3.74 (m, 2H), 3.84 (dd, *J* = 12.6, 6.8 Hz, 1H), 5.15–5.28 (m, 1H), 5.91 (s, 2H), 6.97–7.04 (m, 2H), 7.22–7.34 (m, 2H), 7.40 (ddd, *J* = 8.3, 7.2, 1.2 Hz, 1H), 7.53–7.64 (m, 3H), 8.01 (d, *J* = 8.2 Hz, 1H), and 8.18 (d, *J* = 8.2 Hz, 1H).  $^{13}\text{C}$  NMR (126 MHz, methanol- $d_4$ ):  $\delta$  ppm 31.90, 45.75, 50.69, 52.98, 53.64, 105.77, 111.75, 115.30, 120.16, 123.02, 125.48, 126.72, 126.98, 129.14, 130.02, 131.75, 133.22, 135.30, 135.39, 136.14, 140.17, and 149.84. Monoisotopic mass 376.15,  $[\text{M} + \text{H}]^+ = 377.2$ . HRMS calcd for  $\text{C}_{22}\text{H}_{22}\text{Cl}_2\text{N}_4$ , 377.1533; found, 377.1489.

**(S)-1-(3-Chlorobenzyl)-N-(pyrrolidin-2-ylmethyl)-1H-pyrrolo[3,2-c]quinolin-4-amine Hydrochloride 10.** White solid, overall yield 52%,  $t_{\text{R}} = 4.52$  min, mp 172–174  $^\circ\text{C}$ ,  $\text{C}_{23}\text{H}_{24}\text{Cl}_2\text{N}_4$ , MW 427.37.  $^1\text{H}$  NMR (500 MHz, methanol- $d_4$ ):  $\delta$  ppm 1.92–1.99 (m, 1H), 2.07–2.15 (m, 1H), 2.17–2.25 (m, 1H), 2.37–2.46 (m, 1H), 3.35–3.43 (m, 1H), 3.45–3.53 (m, 1H), 4.10–4.20 (m, 2H), 4.21–4.28 (m, 1H), 5.83 (s, 2H), 6.96–7.00 (m, 2H), 7.19–7.30 (m, 2H), 7.35 (t, *J* = 7.7 Hz, 1H), 7.44 (d, *J* = 3.1 Hz, 1H), 7.52–7.57 (m, 2H), 7.90 (d, 1H), and 8.20 (d, *J* = 8.3 Hz, 1H).  $^{13}\text{C}$  NMR (126 MHz, methanol- $d_4$ ):  $\delta$  ppm 24.28, 29.07, 44.40, 46.73, 53.64, 60.33, 105.52, 111.70, 115.16, 120.19, 122.89, 125.49, 126.63, 126.96, 129.11, 129.90, 131.73, 133.23, 135.09, 135.19, 136.07, 140.10, and 150.26. Monoisotopic mass 390.16,  $[\text{M} + \text{H}]^+ = 391.1$ . HRMS calcd for  $\text{C}_{23}\text{H}_{24}\text{Cl}_2\text{N}_4$ , 391.1689, found, 391.1672.

**General Procedure for Preparation of Compounds 13–21.** Compound **2c** (170 mg, 0.52 mmol, 1 equiv) was suspended in acetonitrile (12 mL), followed by addition of TEA (0.290 mL, 2.08 mmol, 4 equiv). Next, the respective secondary amine (1.56 mmol, 3 equiv) was added. The reaction was heated in a microwave reactor at 140  $^\circ\text{C}$  for 7 h. The solvent was evaporated, and the crude products were purified using  $\text{CH}_2\text{Cl}_2/\text{MeOH}$  (compounds **13–15**) or ethyl acetate (AcOEt)/hexane (Hex) (compounds **16–21**) as the developing solvent. The obtained product was converted into HCl salt of secondary amine upon overnight treatment with 1 M methanolic solution of HCl and subsequent filtration.

**1-(3-Chlorobenzyl)-4-(piperazin-1-yl)-1H-pyrrolo[3,2-c]quinoline Hydrochloride (16) PZ-1922.** White solid, overall yield 55%,  $t_{\text{R}} = 4.29$  min, mp 144–146  $^\circ\text{C}$ ,  $\text{C}_{22}\text{H}_{24}\text{Cl}_2\text{N}_4\text{O}$ , Anal. Calcd for  $\text{C}_{22}\text{H}_{22}\text{Cl}_2\text{N}_4 \times \text{H}_2\text{O}$ : C, 61.26; H, 5.61; N, 12.99. Found: C, 61.27; H, 5.82; N, 12.81. MW 431.36.  $^1\text{H}$  NMR (500 MHz, methanol- $d_4$ ):  $\delta$  ppm 3.60–3.65 (m, 4H), 4.36–4.42 (m, 4H), 6.00 (s, 2H), 7.03–7.07 (m, 2H), 7.26–7.35 (m, 3H), 7.47 (ddd, *J* = 8.4, 7.2, 1.1 Hz, 1H), 7.67 (ddd, *J* = 8.4, 7.2, 1.2 Hz, 1H), 7.73 (d, *J* = 3.4 Hz, 1H), and 8.10–8.14 (m, 2H).  $^{13}\text{C}$  NMR (126 MHz, methanol- $d_4$ ):  $\delta$  ppm 44.32, 47.64, 53.97, 107.56, 112.52, 115.33, 120.34, 123.22, 125.61, 127.03, 127.26, 129.24, 130.68, 131.83, 133.96, 135.23, 136.19, 137.97, 139.86, and 151.96. Monoisotopic mass 376.15,  $[\text{M} + \text{H}]^+ = 377.2$ . HRMS calcd for  $\text{C}_{22}\text{H}_{22}\text{Cl}_2\text{N}_4$ , 377.1533; found, 377.1565.

**1-(3-Chlorobenzyl)-4-(2,6-diazaspiro[3.4]octan-2-yl)-1H-pyrrolo[3,2-c]quinoline Hydrochloride 20.** White solid, overall yield 46%,  $t_{\text{R}} = 4.57$  min, mp 125–127  $^\circ\text{C}$ ,  $\text{C}_{24}\text{H}_{24}\text{Cl}_2\text{N}_4$ , MW 439.38.  $^1\text{H}$  NMR (500 MHz,  $\text{dmsO}-d_6$ ):  $\delta$  2.32 (t, *J* = 7.5 Hz, 2H), 3.19–3.26 (m, 2H), 3.44–3.56 (m, 2H), 4.74 (dd, *J* = 106.4, 44.0 Hz, 4H), 5.97 (s, 2H), 6.87 *J* = 6.95 (m, 2H), 7.05 (s, 1H), 7.27–7.36 (m, 3H), 7.53 (t, *J* = 7.8 Hz, 1H), 7.77 (d, *J* = 3.1 Hz, 1H), 7.96 (d, *J* = 8.3 Hz, 1H), and 8.19 (d, *J* = 8.4 Hz, 1H).  $^{13}\text{C}$  NMR (126 MHz, methanol- $d_4$ ):  $\delta$  ppm 36.29, 42.22, 45.92, 53.71, 54.34, 106.16, 110.62, 114.80, 119.24, 123.19, 125.50, 126.14, 126.94, 129.15, 130.22, 131.76, 133.35, 135.61, 135.63, 136.15, 140.11, and 149.78. Monoisotopic mass: 402.16,  $[\text{M} + \text{H}]^+ = 403.2$ . HRMS calcd for  $\text{C}_{24}\text{H}_{24}\text{Cl}_2\text{N}_4$ , 403.1689; found, 403.1701.

**1-(3-Chlorobenzyl)-4-(piperidin-4-yl)-1H-pyrrolo[3,2-c]quinoline Hydrochloride 23.** Compound **22** (70 mg, 0.17 mmol, 1 equiv) was dissolved in 3 mL of MeOH and 10% Pd/C (25 mg, 30% weight) was subsequently added. The mixture was stirred under a hydrogen atmosphere at room temperature for 2 h. Then, the mixture was filtered through Celite, which was rinsed three times with MeOH. The solvent was evaporated, and the obtained product was converted into HCl salt of secondary amine upon overnight treatment with 1 M methanolic solution of HCl and subsequent filtration.

White solid, overall yield 47%,  $t_{\text{R}} = 4.32$  min, mp 180–182  $^\circ\text{C}$ ,  $\text{C}_{23}\text{H}_{23}\text{Cl}_2\text{N}_3$ , MW 412.36.  $^1\text{H}$  NMR (500 MHz, methanol- $d_4$ ):  $\delta$  ppm 2.38 (d, *J* = 13.8 Hz, 2H), 2.68–2.80 (m, 2H), 3.39 (td, *J* = 12.6, 11.9, 2.9 Hz, 2H), 3.69 (d, *J* = 13.1 Hz, 2H), 4.04–4.15 (m, 1H), 6.12 (s, 2H), 7.00–7.07 (m, 1H), 7.12–7.14 (m, 1H), 7.27–7.34 (m, 2H), 7.68 (d, *J* = 3.4 Hz, 1H), 7.75 (t, *J* = 8.3, 7.1, 1.1 Hz, 1H), 7.89 (t, *J* = 8.4, 7.1, 1.2 Hz, 1H), 7.94 (d, *J* = 3.4 Hz, 1H), 8.38 (dd, *J* = 8.6, 1.2 Hz, 1H), and 8.49 (d, *J* = 8.5 Hz, 1H).  $^{13}\text{C}$  NMR (126 MHz, methanol- $d_4$ ):  $\delta$  ppm 28.07, 40.02, 44.93, 53.95, 106.99, 117.63, 121.02, 122.35, 123.62, 125.62, 127.21, 129.39, 129.80, 131.40, 131.90, 136.25, 136.48, 138.54, 139.47, and 157.14. Monoisotopic mass, 375.15;  $[\text{M} + \text{H}]^+ = 376.2$ . HRMS calcd for  $\text{C}_{23}\text{H}_{23}\text{Cl}_2\text{N}_3$ , 376.1580; found, 376.1552.

**In Silico Evaluation. Structures of the Receptors.** The structure of 5-HT<sub>6</sub>R in the complex with agonist serotonin (PDB ID: 7XTB) and MAO-B cocrystallized with the inhibitor safinamide (PDB ID: 2V5Z) were retrieved from the Protein Data Bank.

**Molecular Docking.** The three-dimensional structures of the ligands were prepared using LigPrep v3.6,<sup>44</sup> and the appropriate ionization states at pH = 7.4  $\pm$  1.0 were assigned using Epik v3.4.<sup>45</sup> The Protein Preparation Wizard was used to assign the bond orders and appropriate amino acid ionization states and to check for steric clashes. The receptor grid was generated (OPLS3e force field)<sup>46</sup> by centering the grid box with a size of 10 Å on the cocrystallized ligand. Automated flexible docking was performed using Glide v6.9<sup>47</sup> at the SP level, and eight poses per ligand were generated.

**Molecular Dynamics.** 100 ns-long molecular dynamics (MD) simulations were performed using Schrödinger Desmond software.<sup>48</sup> Each ligand–receptor complex was immersed into a POPC (309.5 K) membrane bilayer, whose position was calculated using the PPM web server (accessed 20 January 2023).<sup>49</sup> The system was solvated by water molecules described by the TIP4P potential, and the OPLS3 force field was used for all atoms. 0.15 M NaCl was added to mimic the ionic strength inside the cell. The output trajectories were hierarchically clustered into 5 groups according to the ligand using the trajectory analysis tool from Schrödinger Suite.

**Quantum Chemical Calculations.** To recognize intramolecular interactions within the PZ-1939, PZ-1771, and PZ-1922 and structural frameworks, the NCIPLOT program was used.<sup>50</sup> First, the density functional theory (DFT) calculations for ligand conformations determined from the MD trajectory (the most populated cluster) with the GAUSSIAN16 package<sup>51</sup> at the B3LYP-D3/cc-pVDZ level<sup>52–55</sup> with the PCM (water) were performed.<sup>56</sup> Wave functions were obtained and further used to generate reduced electron density gradient (RDG) surfaces by using the NCIPLOT program. The NCI (noncovalent interaction) analysis is based on the reduced RDG defined as

$$s(r) = \frac{|\nabla\rho(r)|}{2(\pi)^{13}\rho(r)^{43}}$$

where  $\nabla\rho(r)$  corresponds to a gradient of the electron density. The NCI allows for visualization of both attractive and repulsive interaction regions. To calculate the energy of detected intramolecular interactions, the topological analysis of electron density was carried out in the AIMAll program.<sup>57</sup> The energy of the noncovalent intramolecular bonds detected in the analyzed structures was calculated using the Espinosa equation<sup>58</sup> as follows

$$E_{\text{int}} = 12\nu(r)$$

where  $E_{\text{int}}$  is the energy of the interatomic interaction, and  $\nu(r)$  is the kinetic energy at the bond critical point (BCP).

**Cryo-Electron Microscopy.** The mouse 5-HT<sub>3A</sub> receptor expression, purification, and cryo-EM imaging were performed as previously described with some minor modifications. Briefly, the receptor was produced using a stable and inducible HEK293 cell line. The membranes of harvested cells were solubilized in the detergent C12E9 (Anatrace), and the receptor was purified by affinity purification followed by size-exclusion chromatography. The fractions corresponding to the pentameric receptors were pooled and concentrated to 10 mg/mL. The purified receptor was incubated with the ligand (10 mmol of PZ-1922 or PZ-1939) for 5 min, then 3.0  $\mu\text{L}$  were deposited on glow-discharged (25 mA, 45 s) Copper/Rhodium Quantifoil R1.2/1.3 grids. Grids were blotted (8 s, 100% humidity, 4 °C) and plunged frozen. The best-looking among a set of 6 grids (in terms of particle density and apparent ice thickness) was selected for data collection (see Table S1) on the IBS Glacios microscope equipped with a Gatan K2 Summit camera. Data treatment was done with CryoSPARC, except for the picking step that was performed with crYOLO. After particles were extracted, several rounds of 2D classification, ab initio model reconstruction with 3 classes, and heterogeneous refinement were performed. The best-looking class was subjected to nonuniform refinement. An existing structure of the 5-HT<sub>3A</sub> receptor was rigidly fitted in the 3D reconstruction. The ligands structures, generated within Phenix Elbow, were added in the binding site, and the model was iteratively refined with Isolde, Coot, and Phenix.

**In Vitro Pharmacological Evaluation. 5-HT<sub>6</sub>R Affinity Evaluation. Cell Culture for Radioligand Binding Assays.** HEK293 cells stably expressing human 5-HT<sub>6</sub>R were grown at 37 °C in a humidified atmosphere with 5% CO<sub>2</sub> and grown in Dulbecco's modified Eagle medium (DMEM) containing 10% dialyzed fetal bovine serum and 500  $\mu\text{g}/\text{mL}$  G418 sulfate. For membrane preparation, cells were subcultured in 150 cm<sup>2</sup> flasks, grown to 90% confluence, washed twice with phosphate buffered saline (PBS) prewarmed to 37 °C, and pelleted by centrifugation (200g) in PBS containing 0.1 mM EDTA and

1 mM dithiothreitol. Prior to membrane preparation, pellets were stored at –80 °C.

**Radioligand Binding Assay.** The cell pellets were thawed and homogenized in 10 volumes of assay buffer using an Ultra Turrax tissue homogenizer, centrifuged twice at 35,000g for 15 min at 4 °C, and incubated for 15 min at 37 °C between centrifugation rounds. The composition of the assay buffer was 50 mM Tris–HCl, 0.5 mM EDTA, and 4 mM MgCl<sub>2</sub>. The assays were performed in a total volume of 200  $\mu\text{L}$  in 96-well microtiter plates for 1 h at 37 °C. The process of equilibration was terminated by rapid filtration through Unifilter plates with a 96-well cell harvester, and radioactivity retained on the filters was quantified on a Microbeta plate reader (PerkinElmer, USA). For displacement studies, the assay samples contained 2 nM [<sup>3</sup>H]-LSD (83.6 Ci/mmol, PerkinElmer). Nonspecific binding was defined with 10  $\mu\text{M}$  methiothepine. Each compound was tested at incremental concentrations (10<sup>–10</sup> to 10<sup>–4</sup> M) in triplicate. The inhibition constants ( $K_i$ ) were calculated from the Cheng–Prusoff equation.<sup>59</sup> Results were expressed as the means of results obtained in two independent experiments.

**Evaluation of 5-HT<sub>6</sub>R Antagonist Activity of PZ-1922 at Gs Signaling.** Compounds were examined for their ability to inhibit 5-HT<sub>6</sub>R-operated cAMP production in the presence of 100 nM (EC<sub>80</sub>) 5-carboxamidotryptamine (5-CT). The level of cAMP was measured in 1321N1 cells expressing h5-HT<sub>6</sub>R (PerkinElmer, #ES-316-CF). Total cAMP was measured using the LANCE cAMP detection kit according to the manufacturer's instructions (PerkinElmer, #TRF0263). Cells were incubated with a mixture of compounds for 30 min at room temperature (RT) in a white polystyrene OptiPlate-384 (PerkinElmer, #6007299) microplate. After incubation, the cells were lysed by the addition of 10  $\mu\text{L}$  of cAMP detection buffer, including Eu-cAMP tracer and ULIGHT-anti-cAMP working solution. The plate was incubated at RT for 1 h before measuring the signal with a Tecan multimode plate reader (Infinite M1000 Pro). Compounds were tested in triplicate at eight concentrations in the range from 10<sup>–11</sup> to 10<sup>–4</sup> M.  $K_b$  constants were calculated from Cheng–Prusoff equation<sup>59</sup> adapted to functional assays.

**Determination of 5-HT<sub>6</sub>R Constitutive Activity at Gs Signaling.** cAMP measurement was performed in NG108-15 cells transiently expressing 5-HT<sub>6</sub>R using the Bioluminescence Resonance Energy Transfer (BRET) sensor for cAMP, CAMYEL (cAMP sensor using YFP-Epac-RLuc).<sup>22</sup> NG108-15 cells were cotransfected in suspension with 5-HT<sub>6</sub>R (or empty vector for Mock condition) and CAMYEL constructs, using Lipofectamine 2000, according to the manufacturer's protocol, and plated in white 96-well plates (Greiner), at a density of 80,000 cells per well. 24 h after transfection, cells were washed with PBS containing calcium and magnesium. Coelenterazine H (Molecular Probes) was added at a final concentration of 5  $\mu\text{M}$  and left at room temperature for 5 min. BRET was measured using a Mithras LB 940 plate reader (Berthold Technologies).

**Impact of Compounds on Neurite Growth.** NG108-15 cells were grown in DMEM supplemented with 10% dialyzed fetal calf serum, 2% hypoxanthine/aminopterin/thymidine (Life technologies), and antibiotics. Cells were transfected with plasmids encoding either cytosolic GFP or GFP-tagged 5-HT<sub>6</sub>R in suspension using Lipofectamine 2000 (Life technologies) and plated on glass coverslips. Six hours after transfection, cells were treated with either DMSO (Vehicle), PZ-1922 (1  $\mu\text{M}$ ), or intepirdine (1  $\mu\text{M}$ ) for 24 h. Cells were fixed in 4% paraformaldehyde (PFA) supplemented with 4% sucrose for 10 min. PFA fluorescence was quenched by incubating the cells in PBS containing 0.1 M glycine prior to mounting in Prolong Gold antifade reagent (Thermo Fisher Scientific). Cells were imaged using an AxioImager Z1 microscope equipped with epifluorescence (Zeiss), using a 20 $\times$  objective for cultured cells, and neurite length (index of 5-HT<sub>6</sub>R constitutive activity as Cdk5 signaling) was assessed using the Neuron J plugin of the ImageJ software (NIH).

**Monoamine Oxidase Assays.** Inhibition activity of the evaluated compounds was measured using human recombinant MAO-B and MAO-A (Sigma-Aldrich M7441 and M7316) in the fluorometric method for detecting monoamine oxidase activity. The assay was carried out in a 96-well plate. Two  $\mu\text{L}$  of the appropriate concentrations

of tested compounds in DMSO were added to wells that contained 98  $\mu\text{L}$  of enzyme dilution (0.53 U/mL) in phosphate buffer (50 mM, pH 7.4). After 30 min of preincubation at room temperature, 50  $\mu\text{L}$  of the solution of 800  $\mu\text{M}$  10-Acetyl-3,7-dihydroxyphenoxazine (Cayman Chemical Company 10010469) and 4 U/mL horse radish peroxidase (HRP, Sigma-Aldrich P6782) were added, and enzymatic reaction was started by the addition of 50  $\mu\text{L}$  of 800  $\mu\text{M}$  *p*-tyramine (Alfa Aesar A12220) solution. The signal was measured after 1 h (excitation at 570 nm and emission at 585 nm) using an EnSpire multimode plate reader (PerkinElmer, Inc.). Rasagiline (1  $\mu\text{M}$ ) or clorgyline (1  $\mu\text{M}$ ) were tested as reference compounds for MAO-B and MAO-A inhibitions, respectively.<sup>60,61</sup>

**MAO-B Reversibility Studies.** To investigate the reversibility of MAO-B inhibition, compound **PZ-1922**, rasagiline, and safinamide were tested in concentrations corresponding to their  $\text{IC}_{50}$  values. The experiment was carried out in a 96-well plate. *h*MAO-B was incubated with inhibitors for 30 min, then low concentration of *p*-tyramine (10  $\mu\text{M}$  in wells) and a solution of 10-acetyl-3,7-dihydroxyphenoxazine and HRP (200  $\mu\text{M}$  and 1 U/mL in wells) were added to the plate. The fluorescence signal had been measured in a microplate reader for 22 min, then the concentration of *p*-tyramine was increased to 1 mM. After the addition of *p*-tyramine, fluorescence was measured every 5 min for 5 h in order to monitor the enzymatic reaction product formation.<sup>60–62</sup>

**Ex Vivo Evaluation of Antagonistic Properties of PZ-1922 at 5-HT<sub>3</sub>R.** Isolated guinea pig ileum was employed to test the affinity for 5-HT<sub>3</sub>R and the intrinsic activity of the investigated compound. The tissue was dissected from male guinea pigs previously deprived of food for 24 h but with free access to drinking water. A 15 cm ileum segment was excised from the small intestine of male guinea pigs and immersed into a Krebs solution (NaCl 120 mM, KCl 5.6 mM, MgCl<sub>2</sub> 2.2 mM, CaCl<sub>2</sub> 2.4 mM, NaHCO<sub>3</sub> 19 mM, glucose 10 mM, pH 7.4). After the first 5 cm length closest to the ileocecal junction had been discarded, 2 cm long fragments were cut. Each segment of the ileum was placed in a 20 mL chamber of the tissue organ bath system (Tissue Organ Bath System-750 TOBS, DMT, Denmark) filled with the Krebs solution at 37 °C, pH 7.4, with constant oxygenation (O<sub>2</sub>/CO<sub>2</sub>, 19:1), fixed by the lower end to a rod and by the upper end to the force–displacement transducer. The preparation was allowed to stabilize in organ baths for 60 min under a resting tension of 0.5 g, washing every 15 min with fresh Krebs solution. After the equilibration period, a cumulative concentration–response curve was constructed in each tissue for 5-HT (10 nM to 10  $\mu\text{M}$ ) by the method of van Rossum.<sup>63</sup> The inhibitory effect of compounds was first evaluated by their influence (after 15 min of incubation with the tissue) on the contraction induced by a single administration of 5-HT at the concentration of 3  $\mu\text{M}$  and expressed as a percentage of inhibition of the maximal tension obtained with the contractile agent. **PZ-1922** was then tested by using an additional method. After establishment of the first 5-HT concentration–response curve, washing out the tissue, and stabilization period, the same tissues were subsequently incubated with one of the concentrations of the tested compound for 15 min, and the next cumulative concentration curve for 5-HT was obtained. Only one concentration of the studied compound was tested on each piece of tissue. Concentration–response curves were analyzed using GraphPad Prism 5.0 (GraphPad Software Inc., San Diego, CA, USA), and the antagonistic properties were expressed as  $\text{pD}_2'$  ( $\text{pD}_2'$ —negative logarithm of the molar concentration of antagonist which reduces the effect of an agonist to 50% its maximum).

**Electrophysiological Evaluation of Antagonist Properties of PZ-1922 at 5-HT<sub>3</sub>R.** *m*5HT<sub>3</sub>R was heterologously expressed in *Xenopus* oocytes by microinjection of 2 ng of phenol/chloroform purified mRNA obtained by *in vitro* transcription (mMESSAGE mMACHINE T7 kit, ThermoFisher). Oocytes were surgically removed from anesthetized *Xenopus* females using procedures that conformed to European regulations for animal handling and experiments and were approved by governmental services (authorization APAFIS# 30915-2021040615209331 granted to Christophe Moreau by the Ministère de l'enseignement supérieur, de la recherche et de l'innovation, on 07 April 2021, valid until 6 April 2026).

Two-electrode voltage-clamp recordings have been performed with the Hi-Clamp automate (Multi-Channel Systems). The running buffer was modified from the standard ND96 buffer by removing calcium ions and adding 1 mM EGTA to avoid the activation of endogenous calcium-activated chloride channels. The composition of the buffer was 91 mM Na, 99 mM Cl<sup>−</sup>, 2 mM KCl, 1.8 mM Ca<sup>2+</sup>, 1 mM Mg<sup>2+</sup>, 5 mM HEPES, pH 7.4. Two borosilicate pipets were filled with 3 M KCl. Two 15 s incubations of 5-HT were performed followed by 5 min washing in buffer flow before 2 min incubation with **PZ-1922**. Amplitude of inhibitions was determined by a third 15 s incubation with 5-HT immediately following **PZ-1922** application. 5-HT and **PZ-1922** solution changes were performed by moving the impaled oocytes in continuously stirred 200 mL reservoirs of a 96-well plate. Washings were performed in the wash-station under continuous flow of the running buffer for 5 min. Data were collected in excel files with homemade software by Michel Vivaudou and statistically analyzed with the Prism 8 software (Graphpad). Current amplitudes were normalized from responses after 2 min of incubation in buffer (in the absence of **PZ-1922**).

**In Vivo Pharmacokinetic and Pharmacological Properties of Compound PZ-1922.** *Animals for Pharmacokinetic Assessment, NOR, and T-Maze Test.* A group of 64 adult male Wistar rats (220–250 g) were used for assessment of the pharmacokinetic profile of **PZ-1922**. The animals were purchased from the Animal House at the Faculty of Pharmacy, Jagiellonian University Medical College, Krakow, Poland. During the habituation period, groups of 4 rats were kept in a plastic cage at a controlled room temperature (22 ± 2 °C), humidity (55 ± 10%), and full spectrum cold white light (350–400 lx) on 12 h light/12 h dark cycles (the lights on at 7:00 a.m. and off at 19:00 p.m.) and had free access to standard laboratory pellet and tap water. For the pharmacokinetic study, **PZ-1922** dissolved in water for injection was administered intravenously (*iv*) and intragastrically (*ig*) at a dose of 3 mg/kg. Blood samples were collected at 0 (before injection) and after injection at 5, 15, 30, 60, 120, 240, and 480 min. Blood and brain samples were collected under general anesthesia induced by *ip* injection of 50 mg/kg ketamine plus 8 mg/kg xylazine. Blood samples were taken after animal decapitation into heparinized tubes and immediately centrifuged at 1000g for 10 min, and plasma was collected. The plasma and brain samples were immediately frozen at −80 °C. All experimental procedures were carried out in accordance with EU Directive 2010/63/EU and approved by the I Local Ethics Committee for Experiments on Animals of the Jagiellonian University in Krakow, Poland (no. 347/2019).

For the NOR test, male Sprague–Dawley rats (Charles River, Germany) weighing ~250 g at the arrival were housed in the standard laboratory cages, under standard colony A/C controlled conditions: room temperature 21 ± 2 °C, humidity (40–50%), 12 h light/dark cycle (lights on: 06:00) with *ad libitum* access to food and water. Rats were allowed to acclimate for at least 7 days before the beginning of the experimental procedure. During this week, the animals were handled at least 3 times. Behavioral testing was carried out during the light phase of the light/dark cycle. The experiments were conducted in accordance with the NIH Guide for the Care and Use of Laboratory Animals and were approved by the Ethics Committee for Animal Experiments, Maj Institute of Pharmacology.

For the AD model, adult male Sprague–Dawley rats (Janvier Lab., France) weighing 260–280 g (8 weeks) at the beginning of the experiments were housed 1 week before experiments in a standard animal facility of the University of Montpellier (CECEMA, registration number E34-172-23) (12/12 h light/dark cycle with lights on at 07:00; 21 ± 1 °C, food and water *ad libitum*). All experiments, including sacrifices, were performed in conscious rats between 09:00 and 12:00, during the diurnal period of the circadian rhythm. Male has been preferred over female because the latter may present a confounding factor of the estrous cycle, a parameter that needs to be systematically controlled. Animal procedures were conducted in strict adherence to the European Union Directive of 2010 (2010/63/EU). The National French Animal Welfare Committee and the local committee at the University of Montpellier approved all protocols (authorization:



CEEA-LR-12160). All efforts were made to minimize the number of animals used, potential pain, suffering, and distress.

### Preliminary Pharmacokinetics Evaluation of PZ-1922.

**Materials and Reagents.** HPLC grade methanol and acetonitrile and reagent grade formic acid, hydrochloric acid, potassium dihydrogen phosphate, orthophosphoric acid, and sodium chloride were purchased from Merck (Darmstadt, Germany).

Control blood and brain samples were obtained from adult male Wistar rats. Rats were anesthetized by intraperitoneal injection of 50 mg/kg ketamine plus 8 mg/kg xylazine, and blood samples were collected in heparinized tubes after animal decapitation. The plasma was separated by centrifugation (1000g, 10 min). Plasma and brain were stored at  $-80^{\circ}\text{C}$  pending analysis.

**Sample Treatment.** The plasma and brain sample pretreatment procedures involved acetonitrile precipitation. A 10  $\mu\text{L}$  aliquot of the internal standard (IS, PH002437, Merck, Darmstadt, Germany) working solution (5  $\mu\text{g}/\text{mL}$ ) was added to 100  $\mu\text{L}$  of the collected mice plasma and brain samples, which were then vortex-mixed for 10 s. Thereafter, 200  $\mu\text{L}$  of acetonitrile was added, vortexed during 20 min, and then centrifuged (7840g, 10 min). The supernatant (200  $\mu\text{L}$ ) was then transferred to an insert placed in an autosampler vial, and a 10  $\mu\text{L}$  volume of this was injected onto the analytical column.

Brain samples were thawed before use, and whole brains were weighted and placed in a glass mortar and pestle tissue grinder and homogenized with an appropriate amount of phosphate buffer (pH 7.4) in a 1:5 ratio. Afterward, 100  $\mu\text{L}$  of tissue homogenates was transferred to new Eppendorf tubes and spiked with 10  $\mu\text{L}$  of the internal standard working solution. All samples were stored on ice during the preparation process, followed by procedures similar to those described above.

**Pharmacokinetic Study.** Pharmacokinetic parameters were calculated by a noncompartmental approach from the average concentration values, using Phoenix WinNonlin software (Certara, Princeton, NJ 08540 USA). The first-order elimination rate constant ( $\lambda_z$ ) was calculated by linear regression of the log concentration versus time. The area under the mean plasma and brain concentration versus time curve ( $\text{AUC}_{0\rightarrow t}$ ) was calculated from zero to the last concentration point using the linear trapezoidal rule. The detailed calculations are presented in [Supporting Information](#).

**Behavioral and Biochemical Impact of PZ-1922. Scopolamine-Induced Amnesia in NOR Test in Rats. NOR Procedure.** At least 1 h before the beginning of the experiments, rats were transferred to the experimental room for acclimation. Rats were tested in a dimly lit (25 lx) "open field" apparatus made of dull gray plastic (66  $\times$  56  $\times$  30 cm). After each measurement, the floor was cleaned and dried.

The procedure consisted of habituation to the arena (without any objects) for 5 min, 24 h before the test, which comprised two trials separated by an inter-trial interval (ITI).

For the scopolamine-induced memory impairment paradigm, 1 h ITI was chosen. During the first trial (familiarization T1), two identical objects (A1 and A2) were presented in opposite corners, approximately 10 cm from the walls of the open field. In the second trial (recognition, T2), one of the objects was replaced by a novel one (A = familiar and B = novel). Both trials lasted 3 min, and animals were returned to their home cage after T1. The objects used were glass beakers filled with gravel and plastic bottles filled with sand. The heights of the objects were comparable ( $\sim 12$  cm), and the objects were heavy enough that they could not be displaced by the animals. The sequence of presentations and the location of the objects were randomly assigned to each rat. The animals explored the objects by looking, licking, sniffing, or touching the object while sniffing but not when leaning against, standing, or sitting on the object. Any rat spending less than 5 s exploring the two objects within 3 min of T1 or T2 was eliminated from the study. Exploration time of the objects and the distance traveled were measured using the Any-maze video tracking system. Based on exploration time (E) of two objects during T2, the discrimination index (DI) was calculated according to the formula  $\text{DI} = (\text{EB} - \text{EA}) / (\text{EA} + \text{AB})$ .

Scopolamine, used to attenuate learning, was administered at a dose of 1.25 mg/kg (*ip*) 30 min before the familiarization phase (T1). The compounds PZ-1922 (0.1; 0.3; 1 and 3 mg/kg) and donepezil (1 and 3

mg/kg) were administrated *ip* 60 min before the familiarization phase (T1).

**Drugs.** Scopolamine hydrobromide (Sigma-Aldrich, Germany), donepezil hydrochloride (Abcam, United Kingdom), or PZ-1922 was diluted in distilled water.

**A $\beta$ -Induced Toxicity in T-Maze Test in Rats. Amyloid- $\beta$  Peptide.** A $\beta_{25-35}$  and scrambled A $\beta_{25-35}$  peptides (Eurogentec, France) were dissolved in sterile water (1  $\mu\text{g}/\mu\text{L}$ ) and stored at  $-20^{\circ}\text{C}$ . Since soluble A $\beta$  oligomers correlate better with the progression of the disease,<sup>29</sup> A $\beta_{25-35}$  and scrambled peptides were preaggregated by an *in vitro* incubation at  $37^{\circ}\text{C}$  (4 days) to obtain a solution mainly composed (more than 95%) of a mixture of soluble oligomer species (oA $\beta_{25-35}$ ), as previously characterized.<sup>64</sup>

**Experimental Procedures for oA $\beta_{25-35}$  Model of AD.** As previously detailed,<sup>37,64</sup> to induce the acute model of AD (oA $\beta_{25-35}$  model), rats were divided into three groups. One group had no surgery (Naive group), a second set of animals received an intracerebroventricular (*icv*) injection of incubated scrambled peptide (negative control groups—10  $\mu\text{g}/\text{rat}$ —Sc), and a third set received an *icv* injection of oA $\beta_{25-35}$  (AD groups—10  $\mu\text{g}/\text{rat}$ —A $\beta$ ). The animals were anesthetized with an intraperitoneal (*ip*) injection of a mixture of ketamine and xylazine (80 and 10 mg/kg b.w., respectively). Scrambled peptide and oA $\beta_{25-35}$  were injected directly into the lateral ventricles at a rate of 2  $\mu\text{L}/\text{min}$  using a David-Kopf stereotaxic apparatus (coordinates of injection: AP  $-1$  mm, L  $\pm 1.5$  mm, DV  $-3.5$  mm).

In order to determine the therapeutic potential of the two 5-HT<sub>2R</sub> antagonists (intepirdine (INTEP) and PZ-1922) in AD pathology induced by the *icv* injection of oA $\beta_{25-35}$ , two therapeutic approaches were evaluated.

1—A curative approach: This treatment was started 1 week after the induction of amyloid toxicity (*icv* injection of oA $\beta_{25-35}$ ) and consisted of 2 *ip* injections (1.5 mg/kg per injection) per day for 1 week. On day 14, animals were subjected to a behavioral memory test (T-maze) and sacrificed on day 15 by decapitation.

2—A preventive approach: This treatment was started at the same time as the induction of amyloid toxicity and consisted of implanting *ip*, and during the same anesthetic procedure necessary for the *icv* injection of oA $\beta_{25-35}$ , an osmotic pump (Alzet-EML2, Charles-River, France) which continuously delivered the molecules for 1 week at the dose of 3 mg/kg/day. On day 7, animals were submitted to a behavioral memory test (T-maze) and sacrificed on day 8 by decapitation.

At the time of sacrifice, all hippocampi were dissected out, weighed, and rapidly frozen in liquid nitrogen for Western blot (WB) analysis. Vehicle rats (N-V, Sc-V, A $\beta$ -V groups) received only *ip* injections (or Alzet pump) of vehicle (sterile 0.9% NaCl) and served as negative controls for pharmacological treatments (N-INTEP, N-PZ1922, Sc-INTEP, Sc-PZ1922, A $\beta$ -INTEP, and A $\beta$ -PZ1922 groups).

**Spatial Short-Term Memory Deficits in the T-Maze Test in Rats.** As previously reported, the T-maze test was used to rapidly assess cognitive ability in rats, especially the short-term memory deficits, when performed in two successive sessions.<sup>37,38,64,65</sup> The T-maze consisted of two short arms (A and B), extending from a longer alley (C) and enclosed with high walls. The test involved two trials, separated by 1 h. During the training session, one short arm (B) was closed. Rats were placed at the end of the long alley, allowed to visit the maze for 10 min, and then returned to their home cage. During the test session, which was videotracked (Noldus EthoVisionXT, France), animals were placed in the maze for 2 min, with free access to all arms. The number of visits and time spent in each arm were measured. The results were expressed as the ratio of the time spent in the initially closed novel arm, over the time spent in the previous arm, and as a ratio of the number of entries into the novel arm over the familiar one. The apparatus was cleaned with diluted ethanol (50%) between animals.

**Western Blot Analysis.** Western blot analyses were performed on the whole hippocampus as previously described.<sup>37</sup> All antibodies used are detailed in Table S3. Briefly, after sacrifice, hippocampi were microdissected, weighed, immediately frozen in liquid nitrogen, and stored at  $-20^{\circ}\text{C}$ . Tissues were sonicated (VibraCell; Sonics & Materials, USA) in a lysis buffer<sup>37</sup> and centrifuged ( $4^{\circ}\text{C}$ ). Supernatants were collected, and the protein concentration was measured using a

bicinchoninic Acid (BCA) assay (ThermoFisher Scientific, France). Samples (60  $\mu$ g protein) were separated on SDS-polyacrylamide gels (12%) and transferred to PVDF membranes (Merck-Millipore, France). The membranes were incubated overnight (4 °C) with the primary antibody, washed, and then incubated for 2 h with the appropriate horseradish peroxidase-conjugated secondary antibody. Peroxidase activity was revealed by using enhanced chemiluminescence (ECL) reagents (Luminata-Crescendo, Merck-Millipore). The intensity of the immunoreactive signals was quantified using Image-J software (NIH, Bethesda, MA, USA).  $\beta$ -Tubulin ( $\beta$ -Tub) was used as a loading control for all experiments.

**Statistical Analysis.** Data are presented as box and whiskers (min to max), including the median value. Before each analysis of variance, the Gaussian distribution was evaluated and validated by a Kolmogorov–Smirnov test (GraphPad-Prism 9.0). Nonparametric tests were used (Mann–Whitney & Dunn's) when the distribution was not normal. Two- or one-way ANOVA followed by Tukey's or Dunnett's multiple comparison tests were used for the normally distributed data set and were resumed in Tables S4 and S6.  $P < 0.05$  was considered significant. The number of animals in each group is indicated in the figure legends. Statistical power analysis was calculated using G\*Power.

## ■ ASSOCIATED CONTENT

### SI Supporting Information

The Supporting Information is available free of charge at <https://pubs.acs.org/doi/10.1021/acs.jmedchem.3c01482>.

Synthesis of compounds **22** and **24–26**; characterization data for final compounds **3**, **4**, **6**, **7–9**, **11–15**, **17–19**, **21**, **22**, and **24–26**; UPLC,  $^1\text{H}$  NMR,  $^{13}\text{C}$  NMR spectra of final compounds **5**, **10**, **15–18**, **20**, and **23**; assessment of physicochemical parameters of **PZ-1922**, selectivity screen for **PZ-1922**; *in silico* evaluation of **PZ-1922** in 5-HT<sub>2</sub>R and MAO-B, cryo-EM studies on **PZ-1922** at 5-HT<sub>3</sub>R; pharmacokinetic evaluation of **PZ-1922**, results of the biochemical analysis of the impact of **PZ-1922** and intepirdine on apoptotic processes in the curative and preventive treatments; and results of the biochemical analysis of curative and preventive treatment with **PZ-1922** and intepirdine (PDF)

5-HT<sub>3</sub>R cryo-EM structure with **PZ-1922** (PDB ID: 8CC6; EMDB ID: EMD-16555) 5-HT<sub>3</sub>R cryo-EM structure with **PZ-1939** (PDB ID: 8CC7; EMDB ID: EMD-16557) 5-HT<sub>6</sub> receptor crystal structure (PDB ID: 7XTB PDB) MAO-B crystal structure (PDB ID: 2V5Z PDB) 5-HT<sub>6</sub> receptor complex with **PZ-1922** 5-HT<sub>6</sub> receptor complex with **PZ-1939** 5-HT<sub>6</sub> receptor complex with FPPQ MAO-B complex with **PZ-1922** MAO-B complex with **PZ-1771** SMILE strings of all shown molecules and corresponding biological activity (CSV)

PDB coordinates of 5-HT<sub>6</sub>\_PZ-1922 (PDB)

PDB coordinates of 5-HT<sub>6</sub>\_FPPQ (PDB)

PDB coordinates of 5-HT<sub>6</sub>\_PZ-1939 (PDB)

PDB coordinates of MAO\_PZ-1922 (PDB)

PDB coordinates of MAO\_PZ-1771 (PDB)

## ■ AUTHOR INFORMATION

### Corresponding Author

Pawel Zajdel – Faculty of Pharmacy, Jagiellonian University Medical College, 30-688 Kraków, Poland; [orcid.org/0000-0002-6192-8721](https://orcid.org/0000-0002-6192-8721); Email: [pawel.zajdel@uj.edu.pl](mailto:pawel.zajdel@uj.edu.pl)

### Authors

Katarzyna Grychowska – Faculty of Pharmacy, Jagiellonian University Medical College, 30-688 Kraków, Poland; [orcid.org/0000-0002-2264-251X](https://orcid.org/0000-0002-2264-251X)

- Uriel López-Sánchez – Univ. Grenoble Alpes, CNRS, CEA, IBS, F-38000 Grenoble, France
- Mathieu Vitalis – Molecular Mechanisms in Neurodegenerative Dementia (MMDN) Laboratory, University of Montpellier, EPHE-PSL, INSERM U1198, 34-095 Montpellier, France
- Geoffrey Canet – Faculty of Medicine, Laval University, CR-CHUQ, G1 V 4G2 Québec City (QC), Canada
- Grzegorz Satala – Maj Institute of Pharmacology, Polish Academy of Sciences, 31-324 Kraków, Poland; [orcid.org/0000-0002-0756-7232](https://orcid.org/0000-0002-0756-7232)
- Agnieszka Olejarz-Maciej – Faculty of Pharmacy, Jagiellonian University Medical College, 30-688 Kraków, Poland
- Joanna Gołębiowska – Maj Institute of Pharmacology, Polish Academy of Sciences, 31-324 Kraków, Poland
- Rafał Kurczab – Maj Institute of Pharmacology, Polish Academy of Sciences, 31-324 Kraków, Poland
- Wojciech Pietruś – Maj Institute of Pharmacology, Polish Academy of Sciences, 31-324 Kraków, Poland
- Monika Kubacka – Faculty of Pharmacy, Jagiellonian University Medical College, 30-688 Kraków, Poland
- Christophe Moreau – Univ. Grenoble Alpes, CNRS, CEA, IBS, F-38000 Grenoble, France; [orcid.org/0000-0002-5463-9593](https://orcid.org/0000-0002-5463-9593)
- Maria Walczak – Faculty of Pharmacy, Jagiellonian University Medical College, 30-688 Kraków, Poland; [orcid.org/0000-0002-5670-9866](https://orcid.org/0000-0002-5670-9866)
- Klaudia Blicharz-Futera – Faculty of Pharmacy, Jagiellonian University Medical College, 30-688 Kraków, Poland; [orcid.org/0000-0001-9243-9042](https://orcid.org/0000-0001-9243-9042)
- Ophélie Bento – IBMM, Université de Montpellier, CNRS, ENSCM, 34-293 Montpellier, France; Institut de Génomique Fonctionnelle, Université de Montpellier, CNRS, INSERM, 34-094 Montpellier, France
- Xavier Bantreil – IBMM, Université de Montpellier, CNRS, ENSCM, 34-293 Montpellier, France; [orcid.org/0000-0002-2676-6851](https://orcid.org/0000-0002-2676-6851)
- Gilles Subra – IBMM, Université de Montpellier, CNRS, ENSCM, 34-293 Montpellier, France; [orcid.org/0000-0003-4857-4049](https://orcid.org/0000-0003-4857-4049)
- Andrzej J. Bojarski – Maj Institute of Pharmacology, Polish Academy of Sciences, 31-324 Kraków, Poland; [orcid.org/0000-0003-1417-6333](https://orcid.org/0000-0003-1417-6333)
- Frédéric Lamaty – IBMM, Université de Montpellier, CNRS, ENSCM, 34-293 Montpellier, France
- Carine Becamel – Institut de Génomique Fonctionnelle, Université de Montpellier, CNRS, INSERM, 34-094 Montpellier, France; [orcid.org/0000-0001-7385-681X](https://orcid.org/0000-0001-7385-681X)
- Charleine Zussy – Molecular Mechanisms in Neurodegenerative Dementia (MMDN) Laboratory, University of Montpellier, EPHE-PSL, INSERM U1198, 34-095 Montpellier, France
- Séverine Chaumont-Dubel – Institut de Génomique Fonctionnelle, Université de Montpellier, CNRS, INSERM, 34-094 Montpellier, France; [orcid.org/0000-0001-6860-6891](https://orcid.org/0000-0001-6860-6891)
- Piotr Popik – Maj Institute of Pharmacology, Polish Academy of Sciences, 31-324 Kraków, Poland; [orcid.org/0000-0003-0722-1263](https://orcid.org/0000-0003-0722-1263)
- Hugues Nury – Univ. Grenoble Alpes, CNRS, CEA, IBS, F-38000 Grenoble, France
- Philippe Marin – Institut de Génomique Fonctionnelle, Université de Montpellier, CNRS, INSERM, 34-094 Montpellier, France; [orcid.org/0000-0002-5977-7274](https://orcid.org/0000-0002-5977-7274)

Laurent Givalois – Molecular Mechanisms in Neurodegenerative Dementia (MMDN) Laboratory, University of Montpellier, EPHE-PSL, INSERM U1198, 34-095 Montpellier, France; Faculty of Medicine, Laval University, CR-CHUQ, G1 V 4G2 Québec City (QC), Canada; CNRS, 75-016 Paris, France

Complete contact information is available at: <https://pubs.acs.org/10.1021/acs.jmedchem.3c01482>

## Notes

The authors declare no competing financial interest.

## ACKNOWLEDGMENTS

The study was financially supported by National Science Center, Poland, (nos. 2016/21/B/NZ7/01742, 2021/43/B/NZ7/02855), Statutory Activity of Jagiellonian University Medical College. Some of the experiments were carried out with equipment cofinanced by the qLIFE Priority Research Area under the program “Excellence Initiative—Research University” at Jagiellonian University. S.C.D. and P.M. were supported by grants from CNRS, Inserm, the Université de Montpellier (no. AAP20REC-FRC02-EcoSero6TSA) and the Agence Nationale de la Recherche (no. ANR-19-CE18-0018). L.G., G.C., C.Z., and M.V. were supported by INSERM, University of Montpellier, and EPHE annual resources (France) and by grants from the Agence Nationale de la Recherche (no. ANR-AAP2022-R22102FF-EpiNeurAge), the Fondation pour la Recherche Médicale (no. MND202003011477-OPA) and the Université de Montpellier (no. MUSE-AAP20REC-FRS09-GAiA). The work used the platforms of the Grenoble Instruct-ERIC center (ISBG; UMS 3518 CNRS-CEA-UGA-EMBL) within the Grenoble Partnership for Structural Biology (PSB), supported by FRISBI (ANR-10-INBS-05-02) and GRAL, financed within the University Grenoble Alpes graduate school (Ecoles Universitaires de Recherche) CBH-EUR-GS (ANR-17-EURE-0003). The electron microscopy facility is supported by the Rhône-Alpes Region, the FRM, the FEDER and the GIS-IBISA. We thank E. Zarkadas and G. Schoehn for their help with cryo-EM. U.L.S. and H.N. were supported by the FRM (EQU202203014691) and the ERC Starting grant 637733.

## ABBREVIATIONS

AChE, acetylcholinesterase; AcOEt, ethyl acetate; AD, Alzheimer’s disease; BBB, blood–brain barrier; BINAP, 2,2’-bis(diphenylphosphino)-1,1’-binaphthyl; BTPP, phosphazene base P1-*t*-Bu-tris(tetramethylene); Casp 3, caspase type 3; CNS, central nervous system; cryo-EM, cryo-electron microscopy; 5-CT, 5-carboxamidotryptamine; DAO, diamine oxidase; GABA, gamma aminobutyric acid; GFAP, glial fibrillary acidic protein; GPCRs, G protein-coupled receptors; *h*ERG, human Ether- $\alpha$ -go-go-Related Gene; 5-HT, serotonin; Hex, hexane; Iba1, ionized calcium-binding adaptor molecule 1; *icv*, intracerebroventricular; *ig*, intragastric; INTEP, intepirdine; *ip*, intraperitoneal; *iv*, intravenous; MAO-B, monoamine oxidase type B; MeOH, methanol; MD, molecular dynamics; NOR, novel object recognition;  $\alpha$ A $\beta$ , oligomeric solution of amyloid- $\beta$  peptide; Pd[(C<sub>6</sub>H<sub>5</sub>)<sub>3</sub>P]<sub>4</sub>, tetrakis (triphenylphosphine) palladium(0); Pd<sub>2</sub>(dba)<sub>3</sub>, tris(dibenzylideneacetone)dipalladium(0); Pd(dppf)Cl<sub>2</sub>, [1,1’-bis(diphenylphosphino)ferrocene]-dichloropalladium(II); PSD-9, postsynaptic density protein 95; SAR, structure activity relationship; SCOP, scopolamine; Scr, scrambled peptide; SEM, standard error of the mean; SERT,

serotonin transporter; SYN, synaptotagmin; *t*-BuOH, *tert*-butanol; TEVC, two-electrode voltage-clamp

## REFERENCES

- (1) Selkoe, D. J. Treatments for Alzheimer’s disease emerge. *Science* **2021**, *373*, 624–626.
- (2) Weinstock, M.; Bejar, C.; Wang, R.-H.; Poltyrev, T.; Gross, A.; Finberg, J. P. M.; Youdim, M. B. H. TV3326, A Novel Neuroprotective Drug with Cholinesterase and Monoamine Oxidase Inhibitory Activities for the Treatment of Alzheimer’s Disease BT—Advances in Research on Neurodegeneration; Riederer, P., Calne, D. B., Horowski, R., Mizuno, Y., Olanow, C. W., Poewe, W., Youdim, M. B. H., Eds.; Springer Vienna: Vienna, 2000; pp 157–169.
- (3) Lecoutey, C.; Hedou, D.; Freret, T.; Giannoni, P.; Gaven, F.; Since, M.; Bouet, V.; Ballandonne, C.; Corvaisier, S.; Malzert Fréon, A.; Mignani, S.; Cresteil, T.; Boulouard, M.; Claeysen, S.; Rochais, C.; Dallemagne, P. Design of donecopride, a dual serotonin subtype 4 receptor agonist/acetylcholinesterase inhibitor with potential interest for Alzheimer’s disease treatment. *Proc. Natl. Acad. Sci. U.S.A.* **2014**, *111* (36), No. E3825.
- (4) Chaumont-Dubel, S.; Dupuy, V.; Bockaert, J.; Becamel, C.; Marin, P. The 5-HT<sub>6</sub> Receptor interactome: new insight in receptor signaling and its impact on brain physiology and pathologies. *Neuropharmacology* **2020**, *172*, 107839.
- (5) Ferrero, H.; Solas, M.; Francis, P. T.; Ramirez, M. J. Serotonin 5-HT<sub>6</sub> receptor antagonists in Alzheimer’s disease: therapeutic rationale and current development status. *CNS Drugs* **2017**, *31*, 19–32.
- (6) Berthou, C.; Hamieh, A. M.; Rogliardo, A.; Doucet, E. L.; Coudert, C.; Ango, F.; Grychowska, K.; Chaumont-Dubel, S.; Zajdel, P.; Maldonado, R.; Bockaert, J.; Marin, P.; Bécamel, C. Early 5-HT<sub>6</sub> receptor blockade prevents symptom onset in a model of adolescent cannabis abuse. *EMBO Mol. Med.* **2020**, *12*, No. e10605.
- (7) Martin, P.-Y.; Doly, S.; Hamieh, A. M.; Chapuy, E.; Canale, V.; Drop, M.; Chaumont-Dubel, S.; Bantreil, X.; Lamaty, F.; Bojarski, A. J.; Zajdel, P.; Eschalier, A.; Marin, P.; et al. mTOR activation by constitutively active serotonin<sub>6</sub> receptors as new paradigm in neuropathic pain and its treatment. *Prog. Neurobiol.* **2020**, *193*, 101846.
- (8) Canale, V.; Grychowska, K.; Kurczab, R.; Ryng, M.; Keeri, A. R.; Satała, G.; Olejarz-Maciej, A.; Koczurkiewicz, P.; Drop, M.; Blicharz, K.; Piska, K.; Pękala, E.; Janiszewska, P.; Krawczyk, M.; Walczak, M.; Chaumont-Dubel, S.; Bojarski, A. J.; Marin, P.; Popik, P.; Zajdel, P. A dual-acting 5-HT<sub>6</sub> receptor inverse agonist/MAO-B inhibitor displays glioprotective and pro-cognitive properties. *Eur. J. Med. Chem.* **2020**, *208*, 112765.
- (9) Lalut, J.; Karila, D.; Dallemagne, P.; Rochais, C. Modulating 5-HT<sub>4</sub> and 5-HT<sub>6</sub> receptors in Alzheimer’s disease treatment. *Future Med. Chem.* **2017**, *9*, 781–795.
- (10) Zajdel, P.; Grychowska, K.; Mogilski, S.; Kurczab, R.; Satała, G.; Bugno, R.; Kos, T.; Gołębiewska, J.; Malikowska-Racia, N.; Nikiforuk, A.; Chaumont-Dubel, S.; Bantreil, X.; Pawłowski, M.; Martinez, J.; Subra, G.; Lamaty, F.; Marin, P.; Bojarski, A. J.; Popik, P. Structure-based design and optimization of FPPQ<sub>4</sub> a dual-acting 5-HT<sub>3</sub> and 5-HT<sub>6</sub> receptor antagonist with antipsychotic and procognitive properties. *J. Med. Chem.* **2021**, *64*, 13279–13298.
- (11) Turner, T. J.; Mokler, D. J.; Luebke, J. Luebke, J. I. Calcium influx through presynaptic 5-HT<sub>3</sub> receptors facilitates GABA release in the hippocampus: in vitro slice and synaptosome studies. *Neuroscience* **2004**, *129*, 703–718.
- (12) Funahashi, M.; Mitoh, Y.; Matsuo, R. Activation of presynaptic 5-HT<sub>3</sub> receptors facilitates glutamatergic synaptic inputs to area postrema neurons in rat brain slices. *Methods Find. Exp. Clin. Pharmacol.* **2004**, *26*, 615–622.
- (13) Dremencov, E.; Weizmann, Y.; Kinor, N.; Gispan-Herman, I.; Yadid, G. Modulation of dopamine transmission by 5-HT<sub>2C</sub> and 5-HT<sub>3</sub> receptors: a role in the antidepressant response. *Curr. Drug Targets* **2006**, *7*, 165–175.
- (14) Rahimian, R.; Fakhfour, G.; Ejtemaei Mehr, S.; Ghia, J. E.; Genazzani, A. A.; Payandemehr, B.; Dehpour, A. R.; Mousavizadeh, K.; Lim, D. Tropisetron attenuates amyloid-beta-induced inflammation

- and apoptotic responses in rats. *Eur. J. Clin. Invest.* **2013**, *43*, 1039–1051.
- (15) Özdemir, Z.; Alagöz, M. A.; Bahçecioğlu, Ö. F.; Gök, S. Monoamine oxidase-B (MAO-B) inhibitors in the treatment of Alzheimer's and Parkinson's disease. *Curr. Med. Chem.* **2021**, *28*, 6045–6065.
- (16) Park, J.-H.; Ju, Y. H.; Choi, J. W.; Song, H. J.; Jang, B. K.; Woo, J.; Chun, H.; Kim, H. J.; Shin, S. J.; Yarishkin, O.; Jo, S.; Park, M.; Yeon, S. K.; Kim, S.; Kim, J.; Nam, M.-H.; Londhe, A. M.; Kim, J.; Cho, S. J.; Cho, S.; Lee, C.; Hwang, S. Y.; Kim, S. W.; Oh, S.-J.; Cho, J.; Pae, A. N.; Lee, C. J.; Park, K. D. Newly developed reversible MAO-B inhibitor circumvents the shortcomings of irreversible inhibitors in Alzheimer's disease. *Sci. Adv.* **2019**, *5*, No. eaav0316.
- (17) Grychowska, K.; Olejarsz-Maciej, A.; Blicharz, K.; Pietruś, W.; Karcz, T.; Kurczab, R.; Koczurkiewicz, P.; Doroz-Płonka, A.; Latacz, G.; Keeri, A. R.; Piska, A.; Satała, G.; Pęgiel, J.; Trybała, W.; Jastrzębska-Więsek, M.; Bojarski, A. J.; Lamaty, F.; Partyka, A.; Walczak, M.; Krawczyk, M.; Malikowska-Racia, N.; Popik, P.; Zajdel, P. Overcoming undesirable hERG affinity by incorporating fluorine atoms: a case of MAO-B inhibitors derived from 1*H*-pyrrolo-[3,2-*c*]quinolines. *Eur. J. Med. Chem.* **2022**, *236*, 114329.
- (18) Vanda, D.; Soural, M.; Canale, V.; Chaumont-Dubel, S.; Satała, G.; Kos, T.; Funk, P.; Fülöpová, V.; Lemrová, B.; Koczurkiewicz, P.; Pękala, E.; Bojarski, A. J.; Popik, P.; Marin, P.; Zajdel, P. Novel Non-Sulfonamide 5-HT<sub>6</sub> receptor partial inverse agonist in a group of imidazo[4,5-*b*]pyridines with cognition enhancing properties. *Eur. J. Med. Chem.* **2018**, *144*, 716–729.
- (19) Deraredj Nadim, W.; Chaumont-Dubel, S.; Madouri, F.; Cobret, L.; De Tautzia, M.-L.; Zajdel, P.; Benedetti, H.; Marin, P.; Morisset-Lopez, S. Physical interaction between neurofibromin and serotonin 5-HT<sub>6</sub> receptor promotes receptor constitutive activity. *Proc. Natl. Acad. Sci. U.S.A.* **2016**, *113*, 12310–12315.
- (20) Grychowska, K.; Satała, G.; Kos, T.; Partyka, A.; Colacino, E.; Chaumont-Dubel, S.; Bantreil, X.; Wesolowska, A.; Pawłowski, M.; Martinec, J.; Marin, P.; Subra, G.; Bojarski, A. J.; Lamaty, F.; Popik, P.; Zajdel, P. Novel 1*H*-pyrrolo[3,2-*c*]quinoline based 5-HT<sub>6</sub> receptor antagonists with potential application for the treatment of cognitive disorders associated with Alzheimer's disease. *ACS Chem. Neurosci.* **2016**, *7*, 972–983.
- (21) Duhr, F.; Délérís, P.; Raynaud, F.; Séveno, M.; Morisset-Lopez, S.; Mannoury La Cour, C.; Millan, M. J.; Bockaert, J.; Marin, P.; Chaumont-Dubel, S. Cdk5 induces constitutive activation of 5-HT<sub>6</sub> receptors to promote neurite growth. *Nat. Chem. Biol.* **2014**, *10*, 590–597.
- (22) Jiang, L. I.; Collins, J.; Davis, R.; Lin, K.-M.; DeCamp, D.; Roach, T.; Hsueh, R.; Rebres, R. A.; Ross, E. M.; Taussig, R.; Fraser, I.; Sternweis, P. C. Use of a cAMP BRET Sensor to characterize a novel regulation of camp by the sphingosine 1-phosphate/G13 pathway. *J. Biol. Chem.* **2007**, *282*, 10576–10584.
- (23) Huang, S.; Xu, P.; Shen, D.-D.; Simon, I. A.; Mao, C.; Tan, Y.; Zhang, H.; Harpsøe, K.; Li, H.; Zhang, Y.; You, C.; Yu, X.; Jiang, Y.; Zhang, Y.; Gloriam, D. E.; et al. Xu, H. E. GPCRs Steer G<sub>i</sub> and G<sub>s</sub> selectivity via TMS-TM6 switches as revealed by structures of serotonin receptors. *Mol. Cell* **2022**, *82*, 2681–2695.e6.
- (24) Binda, C.; Newton-Vinson, P.; Hubálek, F.; Edmondson, D. E.; Mattevi, A. Structure of human monoamine oxidase b, a drug target for the treatment of neurological disorders. *Nat. Struct. Biol.* **2002**, *9*, 22–26.
- (25) Binda, C.; Hubálek, F.; Li, M.; Herzig, Y.; Sterling, J.; Edmondson, D. E.; Mattevi, A. Binding of rasagiline-related inhibitors to human monoamine oxidases: a kinetic and crystallographic analysis. *J. Med. Chem.* **2005**, *48*, 8148–8154.
- (26) Tandarić, T.; Vianello, R. Computational insight into the mechanism of the irreversible inhibition of monoamine oxidase enzymes by the antiparkinsonian propargylamine inhibitors rasagiline and selegiline. *ACS Chem. Neurosci.* **2019**, *10*, 3532–3542.
- (27) Zarkadas, E.; Zhang, H.; Cai, W.; Effantin, G.; Perot, J.; Neyton, J.; Chipot, C.; Schoehn, G.; Dehez, F.; Nury, H. The binding of palonosetron and other antiemetic drugs to the serotonin 5-HT<sub>3</sub> receptor. *Structure* **2020**, *28*, 1131–1140.e4.
- (28) Basak, S.; Kumar, A.; Ramsey, S.; Gibbs, E.; Kapoor, A.; Filizola, M.; Chakrapani, S. High-resolution structures of multiple 5-HT<sub>3A</sub>R-setron complexes reveal a novel mechanism of competitive inhibition. *Elife* **2020**, *9*, No. e57870.
- (29) Selkoe, D. J.; Hardy, J. The amyloid hypothesis of Alzheimer's disease at 25 years. *EMBO Mol. Med.* **2016**, *8*, 595–608.
- (30) Gruden, M. A.; Davidova, T. B.; Malisaukas, M.; Sewell, R. D. E.; Voskresenskaya, N. I.; Wilhelm, K.; Elistratova, E. I.; Sherstnev, V. V.; Morozova-Roche, L. A. Differential neuroimmune markers to the onset of Alzheimer's disease neurodegeneration and dementia: autoantibodies to Aβ<sub>25–35</sub> oligomers, S100b and neurotransmitters. *J. Neuroimmunol.* **2007**, *186*, 181–192.
- (31) Kaneko, I.; Morimoto, K.; Kubo, T. Drastic neuronal loss *in vivo* by beta-amyloid racemized at ser(26) residue: conversion of non-toxic [D-ser(26)]beta-amyloid 1–40 to toxic and proteinase-resistant fragments. *Neuroscience* **2001**, *104*, 1003–1011.
- (32) Pike, C. J.; Burdick, D.; Walencewicz, A. J.; Glabe, C. G.; Cotman, C. W. Neurodegeneration induced by beta-amyloid peptides in vitro: the role of peptide assembly state. *J. Neurosci.* **1993**, *13*, 1676–1687.
- (33) Yankner, B. A.; Duffy, L. K.; Kirschner, D. A. Neurotrophic and neurotoxic effects of amyloid beta protein: reversal by tachykinin neuropeptides. *Science* **1990**, *250*, 279–282.
- (34) Yamada, K.; Nabeshima, T. Animal Models of Alzheimer's Disease and Evaluation of Anti-Dementia Drugs. *Pharmacol. Ther.* **2000**, *88*, 93–113.
- (35) Varadarajan, S.; Kanski, J.; Aksenova, M.; Lauderback, C.; Butterfield, D. A. Different Mechanisms of oxidative stress and neurotoxicity for Alzheimer's Aβ<sub>1–42</sub> and Aβ<sub>25–35</sub>. *J. Am. Chem. Soc.* **2001**, *123*, 5625–5631.
- (36) Canet, G.; Zussy, C.; Hernandez, C.; Maurice, T.; Desrumaux, C.; Givalois, L. The pathomimetic oAβ<sub>25–35</sub> model of Alzheimer's disease: potential for screening of new therapeutic agents. *Pharmacol. Ther.* **2023**, *245*, 108398.
- (37) Zussy, C.; Brureau, A.; Delair, B.; Marchal, S.; Keller, E.; Ixart, G.; Naert, G.; Meunier, J.; Chevallier, N.; Maurice, T.; Givalois, L. Time-course and regional analyses of the physiopathological changes induced after cerebral injection of an amyloid β fragment in rats. *Am. J. Pathol.* **2011**, *179*, 315–334.
- (38) Pineau, F.; Canet, G.; Desrumaux, C.; Hunt, H.; Chevallier, N.; Ollivier, M.; Belanoff, J. K.; Givalois, L. New selective glucocorticoid receptor modulators reverse amyloid-β peptide-induced hippocampus toxicity. *Neurobiol. Aging* **2016**, *45*, 109–122.
- (39) Pao, P.-C.; Tsai, L.-H. Three decades of Cdk5. *J. Biomed. Sci.* **2021**, *28*, 79–96.
- (40) Maitra, S.; Vincent, B. Cdk5-p25 as a key element linking amyloid and tau pathologies in Alzheimer's disease: mechanisms and possible therapeutic interventions. *Life Sci.* **2022**, *308*, 120986.
- (41) Canet, G.; Zussy, C.; Hernandez, C.; Chevallier, N.; Marchi, N.; Desrumaux, C.; Givalois, L. Chronic glucocorticoids consumption triggers and worsens experimental Alzheimer's disease-like pathology by detrimental immune-modulations. *Neuroendocrinology* **2022**, *112*, 982–997.
- (42) Canet, G.; Pineau, F.; Zussy, C.; Hernandez, C.; Hunt, H.; Chevallier, N.; Perrier, V.; Torrent, J.; Belanoff, J. K.; Meijer, O. C.; Desrumaux, C.; Givalois, L. Glucocorticoid receptors signaling impairment potentiates Amyloid-β oligomers-induced pathology in an acute model of Alzheimer's disease. *FASEB J.* **2020**, *34*, 1150–1168.
- (43) Querfurth, H. W.; LaFerla, F. M. Alzheimer's Disease. *N. Engl. J. Med.* **2010**, *362*, 329–344.
- (44) Schrödinger Release 2017–3: QSite; Schrödinger, LLC: New York, NY, 2017; p 2017.
- (45) Shelley, J. C.; Cholleti, A.; Frye, L. L.; Greenwood, J. R.; Timlin, M. R.; Uchimaya, M. Epik: A software program for pK<sub>a</sub> prediction and protonation state generation for drug-like molecules. *J. Comput.-Aided Mol. Des.* **2007**, *21*, 681–691.
- (46) Harder, E.; Damm, W.; Maple, J.; Wu, C.; Reboul, M.; Xiang, J. Y.; Wang, L.; Lupyan, D.; Dahlgren, M. K.; Knight, J. L.; et al. OPLS3:

A force field providing broad coverage of drug-like small molecules and proteins. *J. Chem. Theory Comput.* **2016**, *12*, 281–296.

(47) Friesner, R. A.; Banks, J. L.; Murphy, R. B.; Halgren, T. A.; Klicic, J. J.; Mainz, D. T.; Repasky, M. P.; Knoll, E. H.; Shelley, M.; Perry, J. K.; Shaw, D. E.; Francis, P.; Shenkin, P. S. Glide: A new approach for rapid, accurate docking and scoring. 1. Method and assessment of docking accuracy. *J. Med. Chem.* **2004**, *47*, 1739–1749.

(48) BowersChow, K. J. D. E.; Xu, H.; Dror, R. O.; Eastwood, M. P.; Gregersen, B. A.; Klepeis, J. L.; Kolossvary, I.; Moraes, M. A.; Sacerdoti, F. D.; Salmon, J. K.; Shan, Y.; Shaw, D. E. Scalable algorithms for molecular dynamics simulations on commodity clusters. In *SC'06: Proceedings of the 2006 ACM/IEEE Conference on Supercomputing*, 2006; p 43.

(49) Lomize, M. A.; Pogozheva, I. D.; Joo, H.; Mosberg, H. I.; Lomize, A. L. OPM database and PPM web server : resources for positioning of proteins in membranes. *Nucleic Acids Res.* **2012**, *40* (D1), 370–376.

(50) Contreras-García, J.; Johnson, E. R.; Keinan, S.; Chaudret, R.; Piquemal, J.-P.; Beratan, D. N.; Yang, W. NCIPLLOT: A Program for plotting non-covalent interaction regions. *J. Chem. Theory Comput.* **2011**, *7*, 625–632.

(51) Frisch, M. J.; Trucks, G. W.; Schlegel, H. B.; Scuseria, G. E.; Robb, M. A.; Cheeseman, J. R.; Scalmani, G.; Barone, V.; Petersson, G. A.; Nakatsuji, H.; Li, X.; Caricato, M.; Marenich, A.; Bloino, J.; Janesko, B. G.; Gomperts, R. In *Gaussian 09*, Revision C.01; Gaussian, Inc.: Wallingford CT, 2009.

(52) Becke, A. D. Density functional Thermochemistry. III. The role of exact exchange. *J. Chem. Phys.* **1993**, *98*, 5648–5652.

(53) Grimme, S.; Antony, J.; Ehrlich, S.; Krieg, H. A consistent and accurate ab initio parametrization of density functional dispersion correction (DFT-D) for the 94 elements H-Pu. *J. Chem. Phys.* **2010**, *132*, 154104.

(54) Dunning, T. H. Gaussian Basis Sets for Use in Correlated Molecular Calculations. I. The atoms boron through neon and hydrogen. *J. Chem. Phys.* **1989**, *90*, 1007–1023.

(55) Kendall, R. A.; Dunning, T. H.; Harrison, R. J. Electron affinities of the first row atoms revisited. systematic basis sets and wave functions. *J. Chem. Phys.* **1992**, *96*, 6796–6806.

(56) Miertuš, S.; Scrocco, E.; Tomasi, J. Electrostatic interaction of a solute with a continuum. A direct utilization of ab initio molecular potentials for the prevision of solvent effects. *Chem. Phys.* **1981**, *55*, 117–129.

(57) Keith, T. A. *AIMAll*; TK Gristmill Software: Overland Park, KS, USA, 2015.

(58) Espinosa, E.; Molins, E.; Lecomte, C. Hydrogen bond strengths revealed by topological analyses of experimentally observed electron densities. *Chem. Phys. Lett.* **1998**, *285*, 170–173.

(59) Cheng, Y.-C.; Prusoff, W. H. Relationship between the inhibition constant ( $K_i$ ) and the concentration of inhibitor which causes 50% inhibition ( $I_{50}$ ) of an enzymatic reaction. *Biochem. Pharmacol.* **1973**, *22*, 3099–3108.

(60) Stöbel, A.; Schlenk, M.; Hinz, S.; Küppers, P.; Heer, J.; Gütschow, M.; Müller, C. E. Dual targeting of adenosine  $A_{2A}$  receptors and monoamine oxidase B by 4*H*-3,1-benzothiazin-4-ones. *J. Med. Chem.* **2013**, *56*, 4580–4596.

(61) Łażewska, D.; Olejarz-Maciej, A.; Reiner, D.; Kaleta, M.; Latacz, G.; Zygmunt, M.; Doroz-Plonka, A.; Karcz, T.; Frank, A.; Stark, H.; Kiec-Kononowicz, K. Dual target ligands with 4-tert-butylphenoxy scaffold as histamine  $H_3$  receptor antagonists and monoamine oxidase B inhibitors. *Int. J. Mol. Sci.* **2020**, *21*, 3411–3431.

(62) Tzvetkov, N. T.; Hinz, S.; Küppers, P.; Gastreich, M.; Müller, C. E. Indazole- and indole-5-carboxamides: selective and reversible monoamine oxidase b inhibitors with subnanomolar potency. *J. Med. Chem.* **2014**, *57*, 6679–6703.

(63) van Rossum, J.; van den Brink, F. Cumulative dose-response curves. I. Introduction to the technique. *Arch. Int. Pharmacodyn. Ther.* **1963**, *143*, 240–246.

(64) Zussy, C.; Brureau, A.; Keller, E.; Marchal, S.; Blayo, C.; Delair, B.; Ixart, G.; Maurice, T.; Givalois, L. Alzheimer's disease related markers, cellular toxicity and behavioral deficits induced six weeks after

oligomeric amyloid- $\beta$  peptide injection in rats. *PLoS One* **2013**, *8*, No. e53117.

(65) Brureau, A.; Zussy, C.; Delair, B.; Ogier, C.; Ixart, G.; Maurice, T.; Givalois, L. Deregulation of hypothalamic-pituitary-adrenal axis functions in an Alzheimer's disease rat model. *Neurobiol. Aging* **2013**, *34*, 1426–1439.

#### NOTE ADDED AFTER ASAP PUBLICATION

After this paper was published ASAP October 5, 2023, author Ophélie Bento was added to the author list. The corrected version was reposted October 20, 2023.